American Mineralogist, Volume 94, pages 578–593, 2009

Thermal decomposition of calcite: Mechanisms of formation and textural evolution of CaO nanocrystals

Carlos Rodriguez-Navarro,* Encarnacion Ruiz-Agudo, Ana Luque, Alejandro B. Rodriguez-Navarro, and Miguel Ortega-Huertas

Departamento de Mineralogia y Petrologia, Universidad de Granada, Fuentenueva s/n, 18002, Granada, Spain

Abstract

Field emission scanning electron microscopy (FESEM), two-dimensional X-ray diffraction (2D-XRD), and transmission electron microscopy coupled with selected area electron diffraction (TEM-SAED) analyses of the reactant/product textural relationship show that the thermal decomposition of Iceland spar single crystals according to the reaction $CaCO_{3(s)} \rightarrow CaO_{(s)} + CO_{2(g)}$ is pseudomorphic and topotactic. This reaction begins with the formation of a mesoporous structure made up of up to four sets of oriented rod-shaped CaO nanocrystals on each rhombohedral cleavage face of the calcite pseudomorph. The four sets formed on $(10\bar{1}4)_{calcite}$ display the following topotactic relationships: (1) $(1\bar{2}10)_{calcite}//(110)_{CaO}$; (2) $(\bar{1}104)_{calcite}\perp(110)_{CaO}$; (3) $(\bar{1}018)_{calcite}//(110)_{CaO}$; and (4) $(0\bar{1}14)_{calcite}\perp(110)_{CaO}$; with $[841]_{calcite}//[1\bar{1}0]_{CaO}$ in all four cases. At this stage, the reaction mechanism is independent of P_{CO_2} (i.e., air or high vacuum). Strain accumulation leads to the collapse of the mesoporous structure, resulting in the oriented aggregation of metastable CaO nanocrystals (~5 nm in thickness) that form crystal bundles up to ~1 μm in cross-section. Finally, sintering progresses up to the maximum T reached (1150 °C). Oriented aggregation and sintering (plus associated shrinking) reduce surface area and porosity (from 79.2 to 0.6 m^2/g and from 53 to 47%, respectively) by loss of mesopores and growth of micrometer-sized pores. An isoconversional kinetic analysis of non-isothermal thermogravimetric data of the decomposition of calcite in air yields an overall effective activation energy $E_\alpha = 176 \pm 9$ kJ/mol (for $\alpha > 0.2$), a value which approaches the equilibrium enthalpy for calcite thermal decomposition (177.8 kJ/mol). The overall good kinetic fit with the F_1 model (chemical reaction, first order) is in agreement with a homogeneous transformation. These analytical and kinetic results enable us to propose a novel model for the thermal decomposition of calcite that explains how decarbonation occurs at the atomic scale via a topotactic mechanism, which is independent of the experimental conditions. This new mechanistic model may help reinterpret previous results on the calcite/CaO transformation, having important geological and technological implications.

Keywords: Calcite, lime, thermal decomposition, CaO nanocrystals, TEM-SAED, oriented aggregation, kinetics, topotactic

Introduction

The thermal decomposition of calcium carbonate plays a role in several geologic processes (Harker and Tuttle 1955; Best 1982; O'Keefe and Ahrens 1989; Grapes 2006) and has important technological implications (Boynton 1980; Rodriguez-Navarro et al. 2005). The reaction follows the equation, $CaCO_{3(s)} \rightarrow CaO_{(s)} + CO_{2(g)}$. This reaction occurs on a small scale during pyrometamorphism (Grapes 2006), and on a large scale at subduction zones and during high-grade metamorphism (Best 1982). It also plays a role in other important natural processes. For example, fault-induced thermal decomposition of calcite resulting in ultralow friction in marble appears to play a role in earthquake development (Han et al. 2007). Impact decarbonation of calcite may have implications in our understanding of meteorite mineral evolution and origin (Barber and Scott 2003), as well as the atmospheric evolution on Earth and climate change during unusual meteorite impact events (e.g., K/T impact event) resulting in massive CO_2 outgassing (O'Keefe and Ahrens 1989).

The thermal decomposition of calcite, commonly called calcining or calcination, has been known to mankind since the advent of pyrotechnology (Elert et al. 2002), and has been the subject of extensive research over the last 100 years (Boynton 1980; Dash et al. 2000; Beruto et al. 2004). Lime (CaO), also called quicklime, unslaked lime, or calcia, has been used for building purposes since prehistory, as exemplified by lime plaster floors discovered at Palestina and Turkey, dated ca. 12 000 years old (Elert et al. 2002). Today, lime is used in agriculture (soil conditioning), food processing, disinfecting and disease control, water treatment, flue-gas desulfuration, producing steel, plastic and glass, and sugar refining (Boynton 1980).

In all technical applications, accurate control of the thermal decomposition of calcium carbonate is necessary to achieve a high-quality product meeting certain required properties (Boynton 1980) such as a high reactivity, which is, in turn, related to particle size, surface area, and porosity of the CaO aggregates

* E-mail: carlosrn@ugr.es

0003-004X/09/0004–578$05.00/DOI: 10.2138/am.2009.3021

(Beruto and Searcy 1976). Numerous factors influence such properties of CaO: e.g., particle size, porosity, defect density, and purity of calcium carbonate (limestone) (Fox and Soria-Ruiz 1970; Boynton 1980; Fuller and Yoos 1987), burning *T* (Maciejewski and Oswald 1985), retention time (Boynton 1980), and P_{CO_2} (Beruto et al. 1984; Wilburn and Sharp 1993). A detailed understanding of the role of these factors on calcium carbonate calcination, along with an accurate knowledge on the kinetics and mechanisms of decomposition, are not only necessary for achieving appropriate technological properties of CaO, but may also contribute to the better understanding of calcite thermal decomposition in nature.

Numerous studies have been performed with the aim of yielding a model for the mechanism(s) of calcium carbonate thermal decomposition, often focusing on its kinetic analysis (e.g., Satterfield and Feakes 1959; Beruto and Searcy 1974; Borgwardt 1985; Criado and Ortega 1992; Dash et al. 2000; Maitra et al. 2007, and reviews by Beruto et al. 2004; Stanmore and Gilot 2005). However, transformation mechanisms derived from kinetic analyses rely on the best fit of analytical results (typically derived from thermal analysis) to a particular mechanistic rate-equation (listed in Table 1), without the actual observation of reactant-product textural relationship(s). This has led to the proposal of several contradictory mechanistic models for the thermal decomposition of calcite (e.g., Maciejewski and Reller 1987; Maitra et al. 2007). Comparatively less work has been performed on the analysis of the textural/mineralogical changes taking place during calcite thermal decomposition, including the reactant/product crystallographic relationship, CaO crystallization, growth, and aggregation/sintering, as well as porosity/surface area evolution. With a few exceptions (e.g., Fischer 1955; Glasson 1961; Spinolo and Anselmi-Tamburino 1989), most of these works analyzed the formation and textural evolution of CaO crystals developed in vacuo or in the presence of inert gases (Beruto and Searcy 1976; Towe 1978; Mikhail et al. 1980; Beruto et al. 1980, 1983, 2004; Powell and Searcy 1982; Dash et al. 2000; Singh et al. 2002), thus apparently lacking a direct relationship with the decomposition of $CaCO_3$ taking place in industrial processes, as well as in nature, which often occurs in air. Finally, only a few works have performed kinetic analyses of the thermal decomposition of calcite complemented with the study of the reactant/product textural relationship (see Beruto et al. 2004 and references therein). Moreover, such studies used a limited number of techniques (typically, conventional scanning electron microscopy, X-ray diffraction, and gas adsorption) that do not enable the complete characterization of the calcite/CaO crystallographic and textural relationship(s) at different scales, and their evolution during the calcination process. This paucity of analytical research has prevented the development of a mechanistic model that can fully explain experimental observations for the calcite/CaO transformation.

Considering that the kinetics and the properties of the solid reaction product of the thermal decomposition of calcium carbonate are interrelated (Beruto et al. 1980), we have studied the textural properties of CaO crystals formed after decomposition in air of Iceland spar single crystals at *T* ranging from 600 up to 1150 °C and compared these results with a kinetic analysis of the thermal decomposition process. Special attention has been paid to elucidate, by means of ex-situ transmission electron microscopy (TEM) and selected-area electron diffraction (SAED) analysis, as well as texture 2D X-ray diffraction (2D-XRD) analysis, if the transformation mechanism involves any structural control by the reactant phase, i.e., topotactic reaction, as well as if the presence of metastable nanocrystalline precursors plays a role in the microstructure evolution of the solid product. This study has been complemented by analysis of in-situ decomposition of calcite in a vacuum following irradiation with the electron beam in the TEM. Ex-situ and in-situ TEM-SAED studies, in combination with 2D-XRD analyses, have enabled us to disclose the actual topotactic relationships between calcite and CaO. Our study demonstrates that this solid-state transformation is independent of the experimental conditions (P_{CO_2}, crystal size, and type of energy, i.e., e^- irradiation or heat, used to activate the decomposition reaction). Furthermore, we show that the collapse of the nascent CaO nanostructure occurs via an oriented attachment mechanism prior to standard sintering. Based on these results, a new model is proposed for the calcite/CaO transformation and the textural evolution of the nanocrystalline product phase.

TABLE 1. Broad classification of solid-state mechanistic rate equations

Rate mechanism		Symbol	$f(\alpha)$
(1) Sigmoid α-*T* curves			
	(a) Prout-Tompkins equation	B_1	$\alpha(1-\alpha)$
(1.1) Nucleation and nuclei growth			
	(a) Random nucleation—Avrami-Erofeev equation I	A_2	$2(1-\alpha)[-\ln(1-\alpha)]^{1/2}$
	(b) Random nucleation—Avrami-Erofeev equation II	A_3	$3(1-\alpha)[-\ln(1-\alpha)]^{2/3}$
	(c) Random nucleation—Avrami-Erofeev equation III	A_4	$4(1-\alpha)[-\ln(1-\alpha)]^{3/4}$
(2) Acceleratory α-*T* curves			
	(a) Exponential law	E_1	α
(3) Deceleratory α-*T* curves			
(3.1) Reaction order			
	(a) First order—Unimolecular decay law	F_1	$(1-\alpha)$
	(b) Second order	F_2	$(1-\alpha)^2$
	(c) Third order	F_3	$0.5(1-\alpha)^3$
(3.2) Diffusion mechanism			
	(a) One dimensional transport	D_1	$0.5\,\alpha^{-1}$
	(b) Two dimensional transport (cylindrical geometry)	D_2	$[-\ln(1-\alpha)]^{-1}$
	(c) Three dimensional diffusion, spherical symmetry—Jander equation	D_3	$(3/2)(1-\alpha)^{2/3}[1-(1-\alpha)^{1/3}]^{-1}$
	(d) Three dimensional diffusion, spherical symmetry—Ginstling-Brounshtein equation	D_4	$(3/2)[(1-\alpha)^{-1/3}-1]^{-1}$
(3.3) Phase-boundary reaction			
	(a) Two dimensional (cylindrical geometry)	R_2	$2(1-\alpha)^{1/2}$
	(b) Three dimensional (spherical geometry)	R_3	$3(1-\alpha)^{2/3}$

MATERIALS AND EXPERIMENTAL METHODS

Calcination of calcite crystals

Optical quality calcite crystals (Iceland spar, from Mexico) were cleaved using a blade to obtain millimeter-sized (ca. 3 × 2 × 1 mm) single crystals. Crystals were subsequently calcined in an air-ventilated electric furnace (Select-Horn, Selecta). The furnace *T* control was calibrated using substances whose melting points are well known (KI at 682 °C; KCl at 770 °C; NaCl at 800 °C; Na_2CO_3 at 851 °C; Na_2SO_4 at 884 °C; and NaF at 980 °C). Errors were on the order of ±5 °C in the working *T* interval. The oven was heated from 25 °C up to the target *T* at a rate of 2 °C/min. Once each target *T* was reached, a retention time of 30 min was used before reaching the next target *T* (at 50 °C increments from 600 up to 1150 °C). Samples were collected after the 30 min soaking time at each target *T*, introduced in dry N_2 atmosphere vials, cooled to room *T* and weighed. The fraction decomposed, α, was calculated as follows: $\alpha = (m_i - m_t)/(m_i - m_f)$, where m_i and m_f are the initial and final masses in milligrams, respectively, and m_t is the mass at the specific time, *t*, or temperature, *T*. Following weighing, the samples were introduced again in dry N_2 atmosphere vials before further analysis.

Mineralogical and textural analysis of the samples

Analysis of the phase evolution with calcination *T* was performed by powder X-ray diffraction (XRD) using a Philips PW-1710 diffractometer with Cu*K*α radiation (λ = 1.5405 Å). Data were collected from 20 to 80 °2θ, at a counting rate of 0.03 °2θ s^{-1}. Additionally, calcite single crystals (pseudomorphs) subjected to the above mentioned thermal treatment were placed in the Philips PW-1710 diffractometer chamber with their $\{10\bar{1}4\}$ cleavage plane parallel to the sample holder and XRD patterns were collected.

Pole figures describing the 3D orientation relationships between calcite pseudomorphs and product lime crystals were determined using an X-ray single-crystal diffractometer equipped with an area detector (D8 SMART APEX, Bruker). For these 2D-XRD experiments, the working conditions were Mo*K*α (λ = 0.7093 Å), 50 kV, 30 mA, a pin-hole collimator of 0.5 mm in diameter, and an exposure time of 20 s per frame. Iceland spar pseudomorphs were measured by reflection (diffractometer ω and 2θ angles were set at 10 and 20°, respectively) resting flat on one of the cleavage rhombohedral faces. A set of frames (2D diffraction patterns) was registered while rotating the sample around φ angle (a frame every 5°; a total of 36 frames). Pole densities for the strongest calcite reflections (104, 110, 113, 202, 018, and 116) and lime reflections (111, 200, 220, and 222) were calculated and displayed in stereographic projection using the XRD2DScan software (Rodriguez-Navarro 2007). Each pole figure displays the intensity variation of a given *hkl* reflection as a function of the sample orientation. From these plots, the 3D orientation of associated {*hkl*} faces can be observed. Due to experimental constraints during 2D-XRD data collection, pole figures only represent planes with ρ < 85° [where ρ is the angle between a given (*hkl*) face and the plane of projection]. Note that this is the first time this type of analysis has been performed on calcined calcite crystals.

The evolution of CaO crystallite size with calcination *T* was calculated from peak broadening analysis. The XPowder software package (Martin-Ramos 2004) was used for XRD patterns background subtraction and $K\alpha_2$ stripping, as well as for implementing instrumental broadening correction and peak profile fitting (convolution with either Gaussian, Lorentzian, and/or pseudo-Voight functions). A pseudo-Voight function was finally selected for crystallite size determination using Williamson-Hall plots. The Lorentzian contribution to the pseudo-Voight was generally over 90%, confirming that the strain contribution to broadening was minimal (Howard and Preston 1989) upon annealing/sintering of CaO crystals.

Analysis of the shape, size, and ultrastructure of reactant and product phases was performed by means of field emission scanning electron microscopy (FESEM) using a Leo Gemini 1530 and TEM using a Philips CM20, operated at a 200 kV acceleration voltage. For FESEM analysis, single crystal samples heated at different *T* were placed onto carbon-coated sticky stubs before carbon coating. Prior to TEM observations selected samples (i.e., calcined at 600, 700, 750, 800, 850, 1100, and 1150 °C, thus representing initial and full decomposition, as well as initial and final sintering) were gently ground in an agate mortar and dispersed in ethanol, sonicated 60 s, and deposited on Formbar-coated copper grids. TEM observations were performed using a 40 µm objective aperture. SAED patterns were collected using a 10 µm aperture, which allowed collection of diffraction data from a circular area of 0.5 µm in diameter. In situ decomposition of calcite crystals (about 5 µm in size) due to electron beam damage was also observed in the TEM (i.e., high vacuum conditions). The electron flux was maximized using a large (200 µm) condenser aperture and a focused beam spot size of ~200 nm, thus providing an estimated electron flux of ca. 50–70 $A \cdot cm^{-2}$. Under these conditions, full conversion was achieved after ~1 min exposure. Note that under typical working conditions, the electron flux in the Philips CM20 equipped with a LaB_6 cathode is as low as 6–15 $A \cdot cm^{-2}$, nearly a fifth of the maximum it can provide (Klimenkov et al. 2001). A digital image analysis (DIA) of the electron microscopy images was performed using the Scion Image computer code (Scion Corporation). This analysis enabled the quantification of porosity and pore size of calcite pseudomorphs as well as the size of CaO crystals.

N_2 sorption isotherms were obtained at 77 K on a Micromeritics Tristar 3000 under continuous adsorption conditions. Prior to measurement, samples were heated at 220 °C for 2 h and outgassed to 10^{-3} Torr using a Micromeritics Flowprep. Brunauer-Emmett-Teller (BET) analysis (Brunauer et al. 1938) was used to determine the total specific surface area (SSA). The Barrett-Joyner-Halenda (BJH) method (Barrett et al. 1951) was used to obtain pore-size distribution (PSD) curves.

The porosity and PSD of samples (average of 3 Iceland spar crystals and high-*T* pseudomorphs) were evaluated by means of mercury intrusion porosimetry (MIP, Micromeritics Autopore 5410). Data reduction for pore entry size distribution was performed assuming a cylindrical geometry for the pore network. Overall, the combined use of MIP and N_2 sorption (BJH) analyses enabled the quantification of reactant/product PSD in the range 1–100 µm.

Thermogravimetric analysis (TGA)

Decomposition of Iceland spar crystals was studied in a flowing (100 cm^3/min) air atmosphere using a Shimadzu TGA-50H thermogravimetric analyzer equipped with a Mettler-Toledo AX26 Delta Range microbalance. For each run, the temperature was raised from 25 up to 950 °C at different heating rates, β of 2, 5, 10, and 15 K/min. In each measurement a single crystal (ca. 2 × 2 × 1 mm in size) of ~10 mg was placed into a platinum crucible, and weight loss data were collected at regular time intervals. A small sample size/mass was selected to minimize the mass effect associated with an increase in the partial pressure of CO_2 within the porous system of the reacting crystal (Wilburn and Sharp 1993).

Kinetics of thermal decomposition

The kinetic analysis of TGA data was carried out using a multi-heating-rate method: the Flynn, Wall, and Ozawa (FWO) integral isoconversional method (Vyazovkin and Dollimore 1996). This method yields the effective activation energy E_α and pre-exponential factor *A* (i.e., the Arrhenius parameters) at each given conversion α, that are independent of the reaction model $f(\alpha)$. The FWO method involves measuring the temperatures corresponding to fixed values of α from experiments performed at different heating rates, β, and plotting ln(β) against $1/T_\alpha$,

$$\ln(\beta) = \ln\left[A \cdot \frac{f(\alpha)}{d\alpha / dT}\right] - \frac{E_\alpha}{R \cdot T_\alpha} \quad (1)$$

The slopes of such plots give $-E_\alpha/R$. For isoconversional computations, 100 equidistant values of conversion were chosen. The T_α values related to these conversions were found by nonlinear interpolation. The fraction decomposed (α) was calculated from experimental TGA data. Values of $d\alpha/dT$ were calculated for a set of ~100 values of α for each heating rate and smoothed with the method of moving average of 25 terms. The pre-exponential factor *A* was calculated as in Ruiz-Agudo et al. (2007).

Additionally, a model-fitting analysis was performed to determine the most probable $f(\alpha)$ kinetic model consistent with the isoconversional kinetic results, following the methodology outlined in Vyazovkin and Wight (1997). Table 1 lists the mathematical expressions for several functional forms of $f(\alpha)$ used in this analysis (Vyazovkin and Wight 1997; Galwey and Brown 1998).

RESULTS AND DISCUSSION

Phase evolution with *T*: XRD analysis

Thermal decomposition of calcite single crystals resulted in pseudomorphs that fully preserved the external shape of the $\{10\bar{1}4\}$ rhombohedron. This is impressive if one considers that a porosity of 54.2% is generated after full release of CO_2 from calcite (Beruto et al. 2004). Figure 1a shows the degree

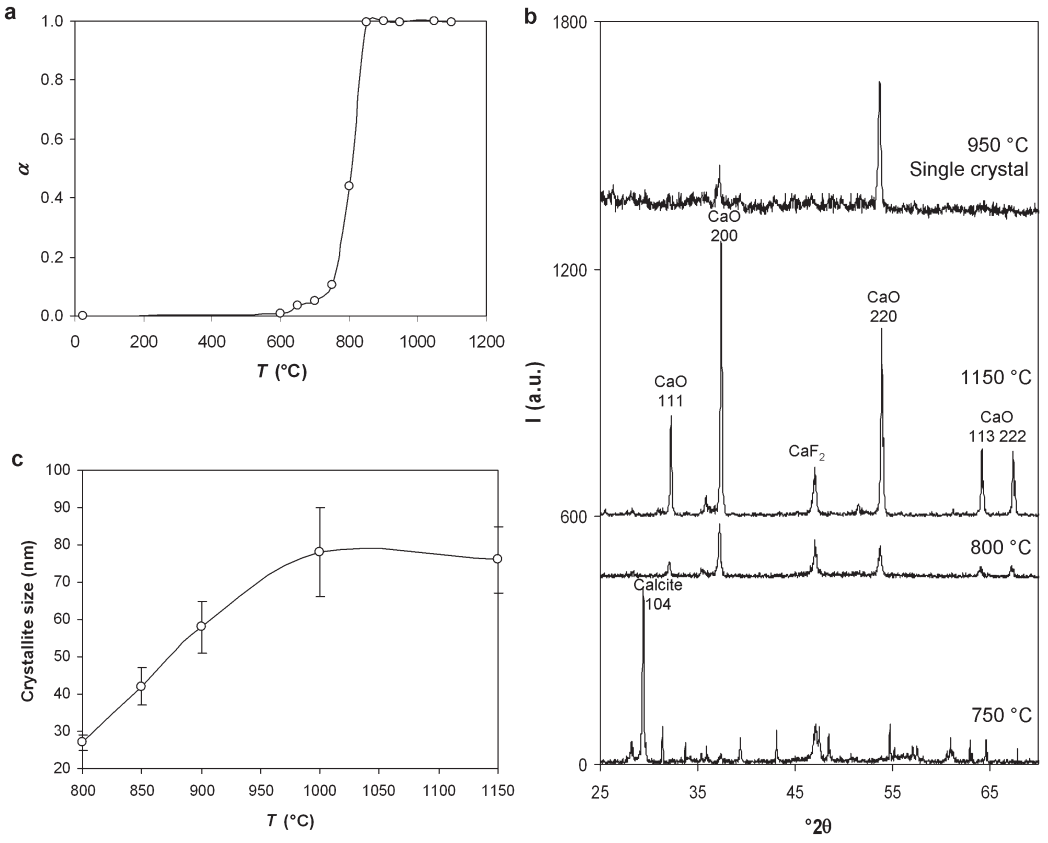

FIGURE 1. (**a**) Degree of conversion α vs. *T* (for constant soaking time); (**b**) XRD patterns of calcite calcined at different *T*: patterns correspond to powders (750, 800, and 1150 °C) and a single crystal (950 °C). Note: CaF_2 was used as an internal standard in powder samples; (**c**) CaO crystallite size determined from XRD peak broadening analysis vs. *T*.

of conversion α vs. *T*. Conversion started at *T* ~ 600 °C, and was completed at ca. 850 °C; i.e., when a loss of 44 wt% corresponding to the stoichiometric CO_2 amount in $CaCO_3$ was achieved. When the partially decomposed pseudomorphs were cut in half, it was observed that the core was a limpid carbonate rhombohedron, surrounded by a brownish shell. This observation suggests that there is crystallographic control in the advancement of the reactant-product interface. It also confirms that the thermal decomposition of carbonates starts at the external surface of a crystal forming a reactant-product interface through which the CO_2 diffuses outside, while the interface moves toward the core of the grain (Beruto et al. 2004).

Figure 1b shows powder XRD patterns of calcite and the product phase formed at different *T*. Small CaO peaks were first detected at 750 °C, corresponding to an amount of 6.2 wt% CaO in the pseudomorph (calculated from α values). At *T* > 800 °C, all calcite Bragg peaks disappeared and the main CaO peaks (111, 200, 220, 311, 222, and 400) were observed up to the maximum target *T*.

The height of CaO Bragg peaks increased with *T*, while peak breadth decreased (Fig. 1b), which suggests that an annealing/sintering process occurred. CaO crystallite size increased with *T* from 27 nm (800 °C) up to 76 nm (1150 °C) (Fig. 1c). This trend is consistent with those reported by Fischer (1955), Glasson (1961), and Dash et al. (2000) for calcite decomposition in air, air/vacuum, and vacuum, respectively. Dash et al. (2000) report crystallite sizes of 17 nm (1000 °C) and 47 nm (1200 °C) following decomposition in vacuum. Spinolo and Anselmi-Tamburino (1989) report a CaO crystallite size of ~36 nm in calcite pseudomorphs decomposed at 547 °C in air, while Beruto et al. (1980) report crystallite sizes of 15 and 38 nm for isothermal (no annealing) decomposition in vacuum and N_2 atmosphere, respectively. In general, the smallest crystallite sizes are observed following decomposition in vacuum as well as at low *T* in air (Spinolo and Anselmi-Tamburino 1989), as observed here. Note that crystallite size values at a given *T* do not depend on the soaking time (Spinolo and Anselmi-Tamburino 1989), which supports the accuracy of our crystallite size measurements.

Non-ground calcite pseudomorphs (i.e., single crystals partially/fully transformed into CaO) yielded XRD patterns where the 220 reflection showed the highest intensity rather than the 200 reflection (Fig. 1b). Beruto and Searcy (1974) have also observed an increase in 220 peak intensity on thermally decomposed {10$\bar{1}$4} calcite single crystals. The authors, in agreement with Singh Dev (1972), conclude that the outer layer is a polycrystalline CaO with the [110] direction oriented preferentially normal to the exposed calcite cleavage plane. However, these authors do not indicate what possible orientation(s) relationship(s) exists between CaO crystals in the polycrystalline outer layer. This is an important omission, as will be shown below.

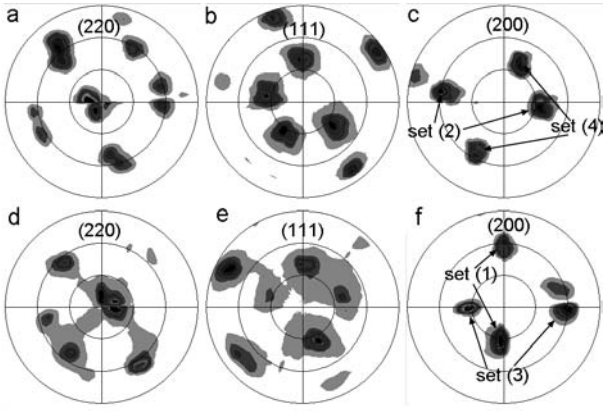

Figure 2. Pole figures of CaO crystals in calcite pseudomorphs calcined at 850 °C (**a**–**c**) and 950 °C (**d**–**f**). Note the well-defined preferred orientation of (220), (111), and (200) planes. Note also the existence of two sets of crystals with (100) planes rotated ca. 75 ° (denoted 2 and 4) and ca. 90° (denoted 1 and 3) with respect to each other resulting in 4 maxima in the pole figures shown in **c** and **f**, respectively. In both pseudomorphs, the (220) planes are tilted ca. 15° with respect to the $(10\bar{1}4)_{calcite}$ cleavage plane (**a** and **d**). As a consequence, the poles of each pair of (111) and (200) planes form an angle of 30° and 60° with respect to the pole of $(10\bar{1}4)_{calcite}$. Due to experimental constrains during XRD data collection, only pole figures corresponding to planes with $\rho < 85°$ are represented. The reference plane (i.e., projection plane) is the cleavage plane of the calcite pseudomorph.

Pole figures of (111), (200), and (220) planes of CaO, obtained from 2D-XRD analysis of non-ground pseudomorphs calcined at 850 °C (Figs. 2a–2c) and 950 °C (Figs. 2d–2f), further confirm the strong preferred orientation of CaO crystals. In particular, $\{110\}_{CaO}$ planes were oriented nearly parallel (~15°) to $\{10\bar{1}4\}_{calcite}$, which is the reference projection plane (Figs. 2a and 2d). Interestingly, Figures 2c and 2f show that the pole figure corresponding to 200 reflections of CaO has four maxima instead of the two expected for a single crystal (or a set of oriented crystals) laying nearly flat on its (110) plane (Note: only planes with $\rho < 85°$ are represented in Fig. 2.) This shows that two sets of CaO crystals developed on the former calcite cleavage plane. These two sets were oriented with respect to each other at an angle of either ~75° (Fig. 2c) or ~90° (Fig. 2f). In both cases, the ρ of two pole maxima was ~30° while that of the other two was ~60° (in agreement with $(110)_{CaO}\wedge(10\bar{1}4)_{calcite}$ ~15°). Similar features were observed in the case of the pole figures of $(111)_{CaO}$: i.e., four maxima at ~75° (Fig. 2b) or ~90° (Fig. 2e). These results suggest that the development of one pair of CaO sets (i.e., oriented at ~75°) is promoted in some cases while in other cases the other pair (i.e., oriented at ~90°) preferentially develops, although their coexistence is consistent with the presence of secondary spots in-between the four maxima in the (200) pole figure (Fig. 2f). Note that the features of the pole figures above discussed did not change with calcination *T* (for $T > 850$ °C). This implies that coarsening of CaO crystals (see below) does not modify the oriented structure formed right

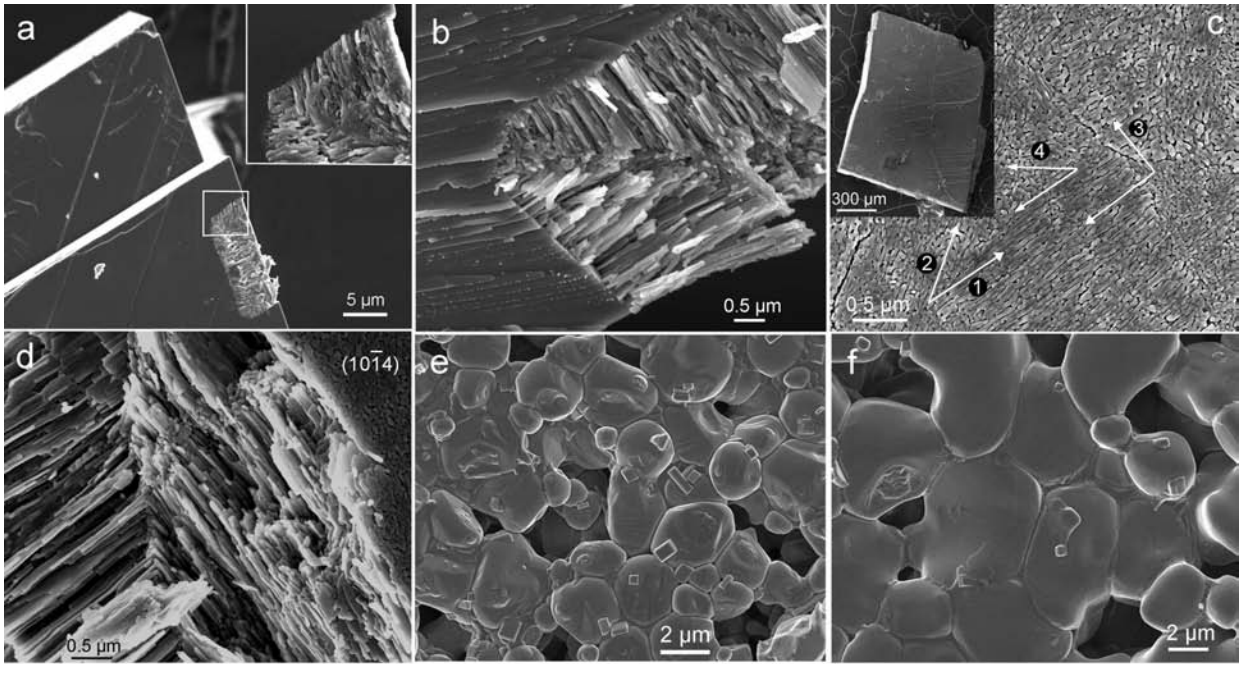

Figure 3. FESEM images of Iceland spar crystals calcined at different temperatures: (**a**) at 700 °C, formation of pockets of oriented CaO crystals are observed with straight edges parallel to the edges of $(10\bar{1}4)_{calcite}$ (detail in inset); (**b**) detail of another pocket similar to that described in **a**, showing two sets of fibrous CaO crystals oriented at ca. 75° (i.e., the acute angle between $\{10\bar{1}4\}_{calcite}$ planes); (**c**) at 850 °C full conversion results in porous calcite pseudomorphs (inset) crisscrossed by cracks and showing four (1–4) sets (bundles) of oriented CaO rods (arrows); (**d**) detail of the cross-section (left) of a calcite pseudomorph calcined at 850 °C. The original $(10\bar{1}4)_{calcite}$ surface is indicated (right); (**e**) sintering of CaO grains at 1000 °C; and (**f**) at 1150 °C.

after calcite decomposition; i.e., that of "nascent" CaO, according to the terminology used by Borgwardt (1985). The specific orientation relationships determined by 2D-XRD analyses also suggest that the calcite/CaO transformation involves a strong crystallographic control.

Textural evolution: FESEM observations

At $T \leq 700$ °C, the most significant microtextural change observed with the FESEM was the formation of cracks (5 up to 20 μm wide), normally parallel to the calcite cleavage plane. It has been reported that decrepitation and macrocrack development typically precede the thermal decomposition of calcite (Boynton 1980; Spinolo and Anselmi-Tamburini 1989). At 700–750 °C, pockets of highly porous aggregates (porosity up to of 34%; average pore size of 15 ± 5 nm, according to DIA results) of oriented rod-shaped CaO nanocrystals (ca. 20 nm in thickness, up to a few micrometers long) were observed at edges of calcite cleavage planes (Fig. 3a). The edges of the pockets were straight and parallel to the edges of the calcite cleavage rhombohedron. This confirms that the reaction front follows specific crystallographic directions. Most importantly, two preferred orientations were observed within these pockets corresponding to two sets of blade- or rod-shaped CaO crystals elongated nearly parallel to the edges of the cleavage plane (inset in Figs. 3a and 3b). The two sets of crystals showed a sharp contact and were oriented at an angle of either ~105° (inset in Fig. 3a) or ~75° (Fig. 3b). Such angles approach the obtuse and acute angles formed by $\{10\bar{1}4\}_{calcite}$ faces (i.e., 105.1 and 74.9°, respectively). These observations are in good agreement with 2D-XRD results showing two sets of CaO crystals on $\{10\bar{1}4\}_{calcite}$ oriented at an angle of ~75° (Fig. 2c). Upon nearly full conversion of calcite at 800–850 °C, an increase in pore-size (up to 73 ± 13 nm) as well as in crystal size (up to 3 μm long, ca. 100 nm in thickness) was observed (Figs. 3c–3d). Pseudomorphs appeared to be less porous (~20% porosity: DIA results) and were criss-crossed by cracks, but still preserved the original morphology of the calcite rhombohedron (inset in Fig. 3c). At these temperatures, rod-shaped CaO crystals had coalesced, still preserving the orientation observed at lower T. In particular, on the cleavage face of the pseudomorph depicted in Figure 3c, up to four sets of rod-shaped CaO crystals were observed. Sets 1 and 3 formed an angle of ~90°, while sets 2 and 4 formed and angle of ~75°. The angle between set 1 and sets 2 and 4 was ~38°, while that of set 3 and sets 2 and 4 was ~52°. The presence of two sets of CaO rods with their longest axis oriented normal to each other, and another two sets at ~75° is fully consistent with 2D-XRD results (Fig. 2). In a cross-section normal to the calcite cleavage plane, two sets of oriented elongated blade-shaped CaO crystals were observed: one with the longest axis nearly parallel to the surface of the pseudomorph, and the other set at an angle of ~90° with respect to the first set. In the cases where CaO crystals were observed aligned nearly normal to the cleavage surface, fractures parallel to the surface developed in the interior of the pseudomorph resulting in the separation of slices a few micrometers thick. Note that the outer surface edges of CaO crystals were rounded and some necks developed between nearby crystals, most probably due to initial sintering. The features shown in Figure 3c have been extensively reported (e.g., Beruto and Searcy 1976). To our knowledge, however, the pockets corresponding to the initial stage of calcination depicted in Figures 3a and 3b, as well as the orientation relationships between different sets of CaO crystals, have not been shown before. These features strongly support a structural control in the calcite/CaO transformation.

Beruto et al. (2004) indicate that the (nano)porous structure developed at the initial stages of the decomposition typically collapses into domains formed by oriented bundles of CaO crystals (as those shown in Figs. 3c and 3d). In large aggregates, a uniform collapse is not possible because different orientations in different collections of rod-shaped CaO crystal aggregates are present, thus the coarsening mechanism is a "small scale equivalent to log jams" (Beruto et al. 1983). The authors conclude that the initial open structure of CaO nanorods is mechanically unstable, thus engendering strains that favor the observed collapse. This is what Beruto et al. (1983) call a "diffusionless repacking" of CaO crystals in the absence of sintering. Although the authors state that the collapse leading to coarsening is mediated by "strong interfacial bonding," they do not explain how this process actually takes place, and how a preferred crystallographic orientation is preserved (or developed) after such a repacking. We will come to this important issue later on when explaining how crystal coarsening occurs. Regarding the observed rounding of edges and neck formation between surface CaO nanorods depicted in Figures 3c and 3d, Beruto et al. (1984) suggest that this is due to limited sintering catalyzed by CO_2. Therefore, it appears that both diffusionless ("repacking") as well as (limited) diffusion-controlled (sintering) coarsening processes occur concomitantly as the decomposition progresses. Overall, these processes lead to an increase in crystal and pore size, as well as to a porosity reduction as shown in by our DIA results.

At 1000 °C, equidimensional, micrometer-sized CaO grains developed showing straight triple boundaries as well as neck contacts (Fig. 3e). These are typical features of a sintering process (Kingery 1960). At the highest target T of 1150 °C, extensive sintering resulted in further CaO crystal coarsening and edge rounding (Fig. 3f). At such a high T, pores enlarged up to sizes ca. 1–5 μm and the porosity was reduced to 9 ± 1% (DIA results). SEM observations by different authors have shown that sintering of CaO crystals typically results in the growth of larger pores at the expenses of the smallest (McClellan and Eades 1970; Obst et al. 1978; Mikhail et al. 1980; Maciejewki and Ostwald 1985).

Ex-situ TEM analysis

Samples heated at $T < 700$ °C do not show any evidence of thermal decomposition. This is most probably due to the low conversion achieved at such T ($\alpha \leq 0.08$), which makes it very difficult to spot a transformed crystal in the TEM. At 750 °C ($\alpha = 0.15$), some calcite pseudomorphs were observed with the $d_{111} = 2.78$ Å, $d_{200} = 2.40$ Å, and $d_{220} = 1.70$ Å strongest reflections of CaO in SAED patterns (Fig. 4a). Such pseudomorphs were highly porous (ca. 46% porosity, with average pore size of 5–10 nm, according to DIA results) and were made up of nanometer-sized prisms or rods (ca. 20–50 nm long and 5 nm in thickness), that were typically arranged in an oriented fashion (Fig. 4b). The preferred orientation of CaO nanocrystals was confirmed by the SAED pattern showing the presence of discrete spots in each Debye ring, along with discrete 104 spots from the remaining

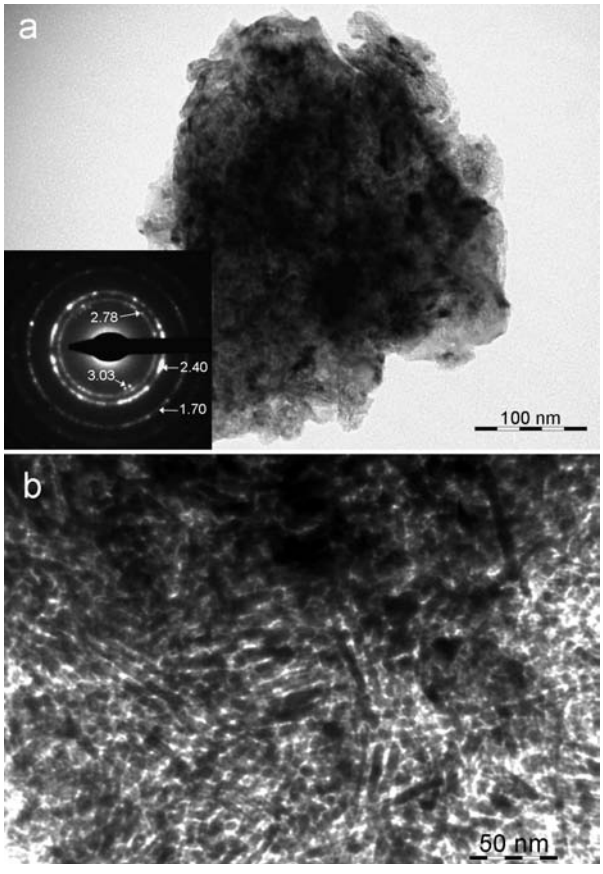

FIGURE 4. TEM images of (**a**) calcite pseudomorph calcined at 750 °C showing SAED corresponding to the [110] zone axis of CaO (inset). Spots corresponding to CaO d_{111} = 2.78 Å; d_{200} = 2.40 Å, and d_{220} = 1.70 Å are observed. Spots corresponding to calcite 104 reflections at 3.03 Å are also present; (**b**) detail of the pseudomorph showing CaO nanocrystals with preferred orientation.

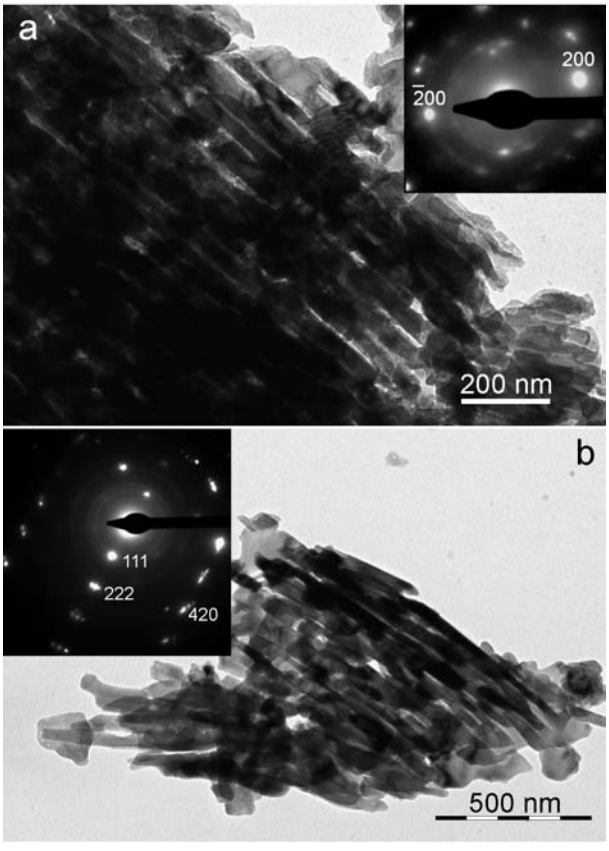

FIGURE 5. TEM images of calcite pseudomorph calcined at 850 °C showing details of CaO crystal aggregates with preferred orientation. SAED patterns evidence orientation in two different directions: (**a**) along the [0$\bar{2}$1] zone axis, and (**b**) along the [$\bar{1}$2$\bar{1}$] zone axis.

calcite reactant (see inset in Fig. 4a). At 850 °C, full conversion into CaO occurred. Pseudomorphs showed a porous structure formed by oriented aggregates of larger (ca. 200–500 nm long and 30 nm in thickness) prismatic CaO crystals (Fig. 5). The sizes of CaO nanocrystals observed with the TEM are thus consistent with XRD peak broadening analysis results, and follow the same coarsening trend shown by FESEM analysis. These crystal sizes are similar to those observed by Towe (1978) and Singh et al. (2002) in the TEM. They are also similar to those calculated by Borgwardt et al. (1986) and Borgwardt (1989) from N_2 sorption measurements (11 nm and up to 180 nm for "nascent" and sintered CaO crystals, respectively), despite the authors' assumption regarding the spherical shape of "nascent" CaO. In equally oriented aggregates (Fig. 5), the porosity was reduced in comparison with that of samples calcined at lower *T* (down to ca. 34% porosity) and the average pore size increased up to ~30 nm. This stage corresponds to the "collapsed" structure reported by Beruto et al. (1983). The preferred orientation of the CaO aggregates was much more evident at this *T*. SAED patterns of [0$\bar{2}$1] and [$\bar{1}$2$\bar{1}$] zone axes (insets in Figs. 5a and 5b, respectively) confirmed such strong preferred orientation. SAED patterns of individual prisms rotated ±45° around their longest axis showed that the CaO crystals were elongated along the [110] direction. This novel finding suggests that the $[110]_{CaO}$ direction plays a critical role in the calcite/CaO transformation process. At 1100 °C, individual micrometer-sized CaO crystals were observed (Fig. 6a). Some of them showed rounded edges, consistent with the advanced sintered texture observed with the FESEM. The CaO grains were single crystals with no visible porosity. Figure 6a shows the [001] zone axis SAED pattern of a large CaO crystal. Note that the *h*00, 0*k*0, and *hk*0 reflections are broad and slightly ellipsoidal, which suggests that some degree of orientation mismatch among CaO crystallites exists. This is confirmed by HRTEM images showing Moiré fringes and orientation mismatching between lattice fringes of nearby CaO crystallites (Fig. 6b). Furthermore, some weak and diffuse Debye rings corresponding to the main CaO reflections were visible. This implies that such a large crystal is formed by an oriented aggregate of the (nano)crystals observed at lower *T*. Porosity is lost and crystals attach along equally oriented faces during aggregation, thus minimizing surface energy. In addition to mechanical strain associated with the differences in molar volume between calcite and CaO, surface energy minimization

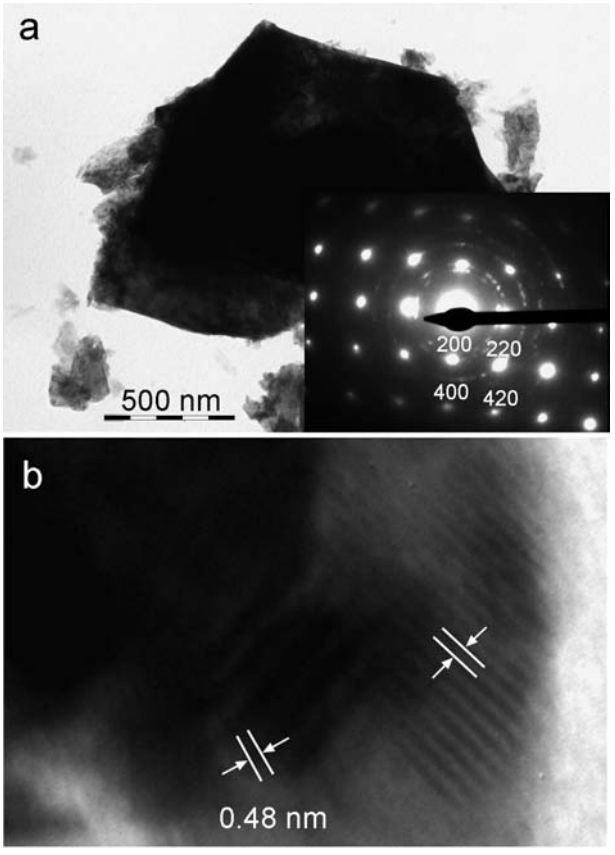

FIGURE 6. CaO crystals in a Iceland spar sample calcined at 1100 °C: (**a**) large CaO crystal oriented along the [001] zone axis (SAED in inset); and (**b**) high-resolution image showing Moiré fringes and orientation mismatching (i.e., non-perfect orientation) between lattice fringes of CaO crystallites in a large CaO crystal.

must be a strong driving force for aggregation in the case of "nascent" CaO nanocrystals due to their high surface/volume ratio. This aggregation should also be facilitated by the oriented texture of nascent CaO crystal rods and the small size of the pores separating these crystals (ca. 5 nm). Such an "oriented aggregation" coarsening mechanism has been proposed to explain crystal growth in solution (Penn and Banfield 1998); however, this is the first time that such a mechanism is proposed to explain solid-state crystal coarsening. Penn and Banfield (1998) report that oriented aggregation typically leads to some degree of mismatching among crystallites. Such mismatching is responsible for the features observed in the SAED pattern and HRTEM image shown in Figure 6. This oriented aggregation mechanism explains why the initial preferred crystallographic orientation is preserved after the diffusionless repacking of CaO nanocrystals. Besides this diffusionless mechanism of crystal coarsening, our electron microscopy observations show that sintering also operates as T increases, apparently being the dominant coarsening mechanism at $T > 850$ °C.

In situ TEM analysis

Decomposition of calcite crystals in situ and in vacuo was observed following exposure to the electron beam in the TEM. Figure 7 shows the effects of beam damage. The calcite crystal in Figure 7a (which was oriented along the [841] zone axis) transformed into an oriented aggregate of CaO crystals, as revealed by the SAED pattern of the calcite/CaO interface (Fig. 7b). The pseudomorph showed the typical mottled texture observed following beam damage of carbonates (Wenk et al. 1983). The SAED pattern in Figure 7b corresponds to the $[1\bar{1}0]$ zone axis of CaO, which includes diffuse spots (arcs) from 111, 220, and 002 (and equivalent) reflections. This SAED pattern shows the following reactant/product orientation relationship: $[841]_{calcite}//[1\bar{1}0]_{CaO}$. Details of the newly formed oriented CaO nanocrystals are shown in Figures 7c and 7d. CaO nanorods were oriented with their longest axis nearly parallel to $(10\bar{1}4)_{calcite}$ [note that the TEM image plane forms an angle of 15° with $(10\bar{1}4)_{calcite}$]. The SAED pattern of the fully transformed pseudomorph (inset in Fig. 7c) is consistent with the presence of four sets of CaO crystals oriented with $[1\bar{1}0]_{CaO}$ parallel to $[841]_{calcite}$, and displaying the following reactant/product orientation relationships: (1) $(1\bar{2}10)_{calcite}//(110)_{CaO}$; (2) $(\bar{1}104)_{calcite}\perp(110)_{CaO}$; (3) $(\bar{1}018)_{calcite}//(110)_{CaO}$; and (4) $(0\bar{1}14)_{calcite}\perp(110)_{CaO}$. Note that the reciprocal vector $220^*_{(3)}$ forms an angle of ~52° with $220^*_{(2)}$ and $220^*_{(4)}$, and an angle of 90° with $220^*_{(1)}$, while $220^*_{(1)}$ forms an angle of ~38° with $220^*_{(2)}$ and $220^*_{(4)}$ (inset in Fig. 7c). The four sets of rod-shaped CaO nanocrystals and their angular relationships are shown in detail in Figure 7d (see also scheme in inset). Note that the most intense diffuse spots in the SAED pattern shown in Figure 7c corresponded to $002_{(3)}$. Such spots were aligned parallel to $1\bar{2}10_{calcite}$ reflections, thus showing the orientation relationship $(\bar{1}018)_{calcite}//(110)_{CaO}$. This orientation should therefore correspond to the most abundant nanorods in Figure 7d, i.e., those noted as set (3). These nanorods formed an angle of ~52° with the two sets with $(110)_{CaO}$ normal to $(\bar{1}104)_{calcite}$ and $(0\bar{1}14)_{calcite}$ [i.e., those noted as (2) and (4), respectively], and an angle of ~90° with the rods displaying the orientation relationship $(1\bar{2}10)_{calcite}//(110)_{CaO}$ [i.e., those noted as (1)]. Overall, in situ TEM-SAED results showing the formation on $(10\bar{1}4)_{calcite}$ of four sets of CaO crystals elongated along [110], two sets parallel to the bisectors of the acute and obtuse angles of the rhombohedral face (and forming an angle of 90°) and two parallel to the edges of the calcite cleavage rhombohedron (forming an angle of ~105 or ~75°) are thus consistent with 2D-XRD results and FESEM observations.

The dimension of pores (ca. 5–10 nm) and CaO crystals (5–10 nm thick, 25–75 nm long) formed in the TEM in vacuo, were very similar to those observed in samples calcined in air at 750 °C (Fig. 4). In contrast to previous knowledge (e.g., Borgwardt 1989), the latter implies that the textural features of nascent CaO aggregates are not dependent on P_{CO_2} (note however that P_{CO_2} influences calcite decomposition temperature and rates, as well as the coarsening of CaO crystals; Zhong and Bjerle 1993; Beruto et al. 2004). Also in contrast to previous knowledge (see review by Beruto et al. 2004), these observations suggest that the reactant crystal size (e.g., millimeter-sized single crystals or micrometer-sized powder analyzed in ex-situ and in-situ TEM, respectively) does not influence the decomposition mechanism. Furthermore, the type of energy (e^- irradiation or heat) used to activate the calcite/CaO transformation does not seem to affect the decomposition reaction mechanisms either. The latter has

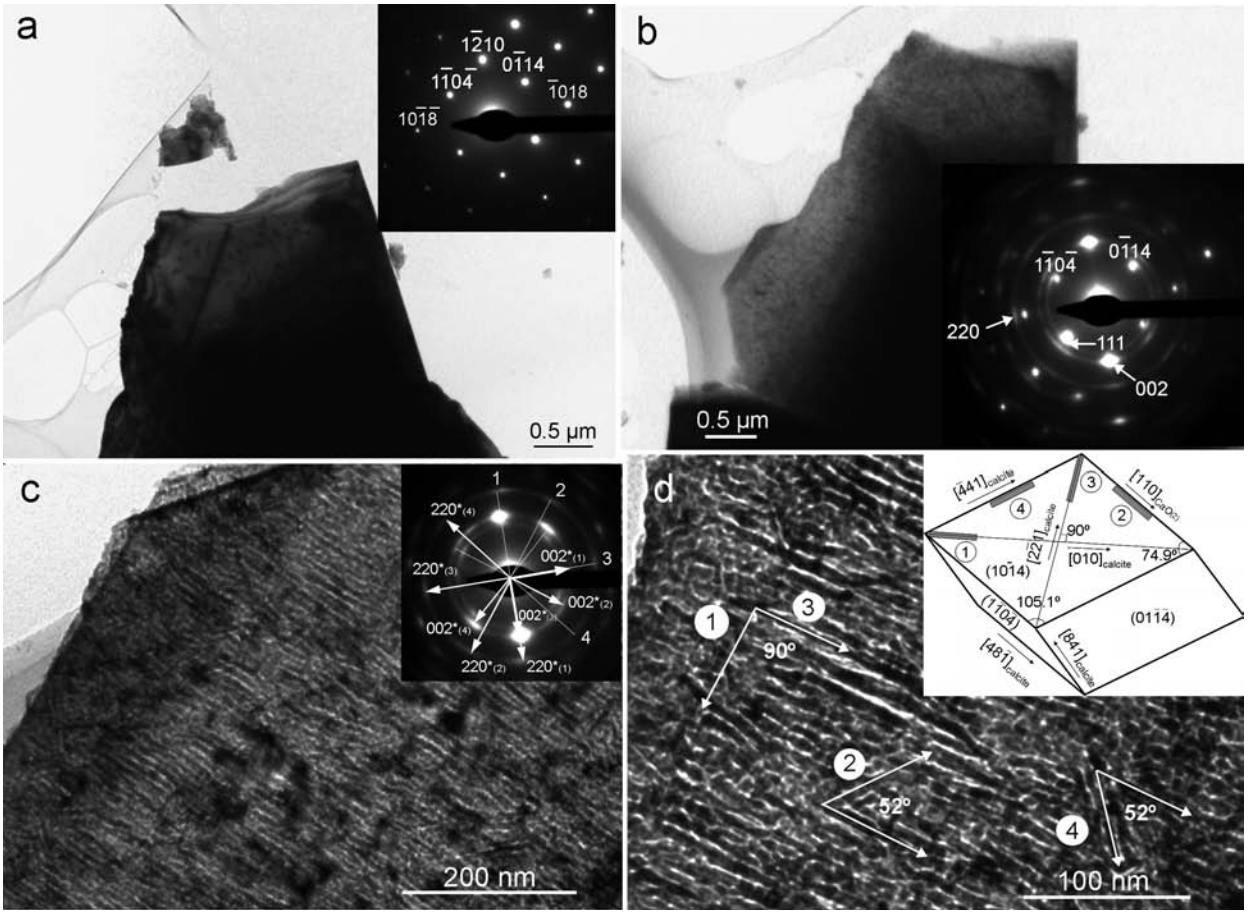

FIGURE 7. Images of a calcite crystal undergoing in situ decomposition in the TEM: (**a**) calcite crystal observed along the [841] zone axis (SAED in inset); the $(10\bar{1}4)$ plane is tilted ~15° with respect to the image plane; (**b**) the same crystal after beam damage showing discrete SAED spots/arcs (inset) corresponding to the 111, 200, and 220 reflections of (four sets of) CaO crystals with different orientation. Some SAED spots from the parent phase are still visible; (**c** and **d**) details of the highly oriented CaO crystals at the edge of the calcite pseudomorph. The $[1\bar{1}0]$ zone axis SAED pattern in **c**, corresponding to a fully transformed pseudomorph, shows the existence of four sets of CaO crystals with the following angular relationships: $220^*_{(1)}\wedge 220^*_{(2)}$ ~52°; $220^*_{(1)}\wedge 220^*_{(4)}$ ~52°; and $220^*_{(1)}\wedge 220^*_{(3)}$ ~90°. Such orientation relationships are shown in detail in **d** for the four sets of CaO crystals. Inset in **d** shows a scheme of the orientation of the four sets of CaO crystals (gray-shaded) formed on $(10\bar{1}4)_{calcite}$. CaO crystals are elongated along [110].

important implications for the understanding of the mechanism of calcite/CaO transformation, since radiolysis of $CO_3^=$ groups by the e^- beam would occur at a sufficiently low temperature as to prevent ion diffusion (Carter and Buseck 1985). Therefore, the mechanism of calcite/CaO transformation must be diffusionless.

Burrage and Pitkethly (1969) and Towe (1978) were the first to observe an orientation relationship among calcite crystals and CaO nanorods following in situ decomposition of the carbonate in the TEM. However, the authors did not reach decisive conclusions regarding the topotactic (or not) nature of such a decomposition process. McTigue and Wenk (1985) also observed the decomposition of calcite into lime following in situ thermal decomposition of calcite in the TEM (using a heating stage). The authors conclude that it was topotactic with $(001)_{CaO}\sim(\bar{1}104)_{calcite}$ and $(\bar{1}\bar{1}1)_{CaO}\sim(0001)_{calcite}$. The carbonate threefold axis thus turned into one of the face centered cubic (fcc) oxide threefold axes. Such orientation relationship is not consistent with our 2D-XRD and TEM-SAED results. McTigue and Wenk (1985) orientation is also not consistent with the XRD results of Singh Dev (1972). The latter found the following topotactic relationship: $(10\bar{1}4)_{calcite}//(110)_{CaO}$; $[010]_{calcite}//[100]_{CaO}$; and $(11\bar{2}0)_{calcite}//(311)_{CaO}$. Singh et al. (2002) recently reported two possible orientation relationships, namely OR1 and OR2, between calcite and CaO crystals formed in situ in the TEM. In the case of OR1, $<\bar{4}41>_{calcite}$ coincides with $<110>_{CaO}$, $(10\bar{1}4)_{calcite}//(\bar{1}11)_{CaO}$, $(01\bar{1}4)_{calcite}//(1\bar{1}1)_{CaO}$, and $(\bar{1}104)_{calcite}//(210)_{CaO}$. Conversely, in the so-called OR2, $<\bar{4}41>_{calcite}$ coincides with $<001>_{CaO}$, $\{\bar{1}100\}_{calcite}//\{110\}_{CaO}$, and $\{10\bar{1}4\}_{calcite}$ are nearly parallel to $\{100\}_{CaO}$. The authors report two pathways for phase transformation: pathway 1 leads to CaO nanocrystals of random orientation, while pathway 2 leads to oriented nanocrystals following OR2. The first pathway implies that the transformation is not always topotactic. However, the preexistence of defects or their development during heating and/or e^- irradiation (e.g., twining) will lead to complex SAED patterns masking the actual topotactic relationship. In fact,

we have observed twining of calcite crystals during the early stages of in situ calcite/CaO transformation leading to spotty Debye rings (similar to those shown by Singh et al. 2002) where the topotactic relationship was partially masked (Fig. 8). Thus, the first pathway proposed by Singh et al. (2002) seems to be an experimental artifact. For the second pathway, Singh et al. (2002) discard OR1 as an effective topotactic route because they think it involves a lot of atomic rearrangement. They therefore conclude that OR2 is the only effective topotactic route for the calcite/CaO transformation in the TEM. In contrast, the orientation relationships we have found are only consistent with one of the features of OR1, i.e., $<\bar{4}41>_{calcite}$ coincides with $<110>_{CaO}$ and one of the orientation relationships reported by Singh Dev (1972), i.e., $[010]_{calcite}//[001]_{CaO}$ (only in the case of set 3 in Fig. 7). It follows that none of the topotactic relationships so far proposed can fully explain the orientation relationships shown by our 2D-XRD, FESEM, and TEM-SAED analyses. Note that all topotactic relationships proposed in the past were based on the analysis of the calcite/CaO transformation using a single technique (either TEM—collecting SAED patterns for a limited number of orientations—or conventional XRD). Furthermore, previous topotactic models do not explain how this transformation occurs at the atomic scale. A new atomic-scale model for the topotactic transformation between calcite and CaO that accounts for all our experimental observations will be presented and discussed in the final section of this paper.

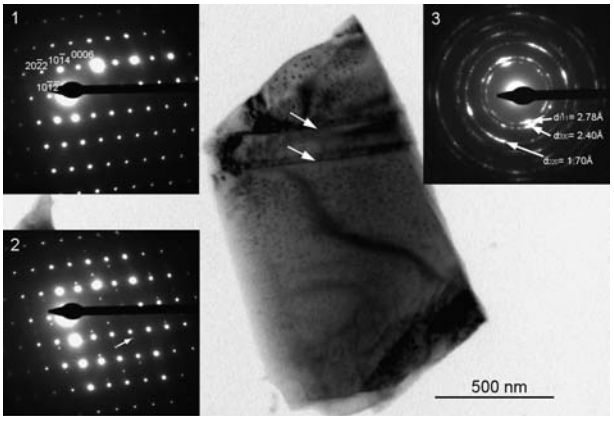

FIGURE 8. Calcite crystal oriented along the [010] zone axis (SAED pattern in inset 1) undergoing twining (arrow pair) at the initial stages of e^- irradiation (see new set of spots, i.e., arrow, in inset 2) and subsequent transformation into an aggregate of CaO crystals showing a SAED pattern with spotty, nearly continuous Debye rings (inset 3). Note however that a preferred orientation of CaO crystals is still detectable by the brighter spots in the Debye rings.

Surface area, porosity, and pore-size distribution evolution

N_2 sorption isotherms are shown in Figure 9a. The un-calcined Iceland spar crystals showed a type-II isotherm (i.e., without hysteresis loop), typical of non-porous solids (Sing et al. 1985). This is consistent with the low surface area of the non-porous

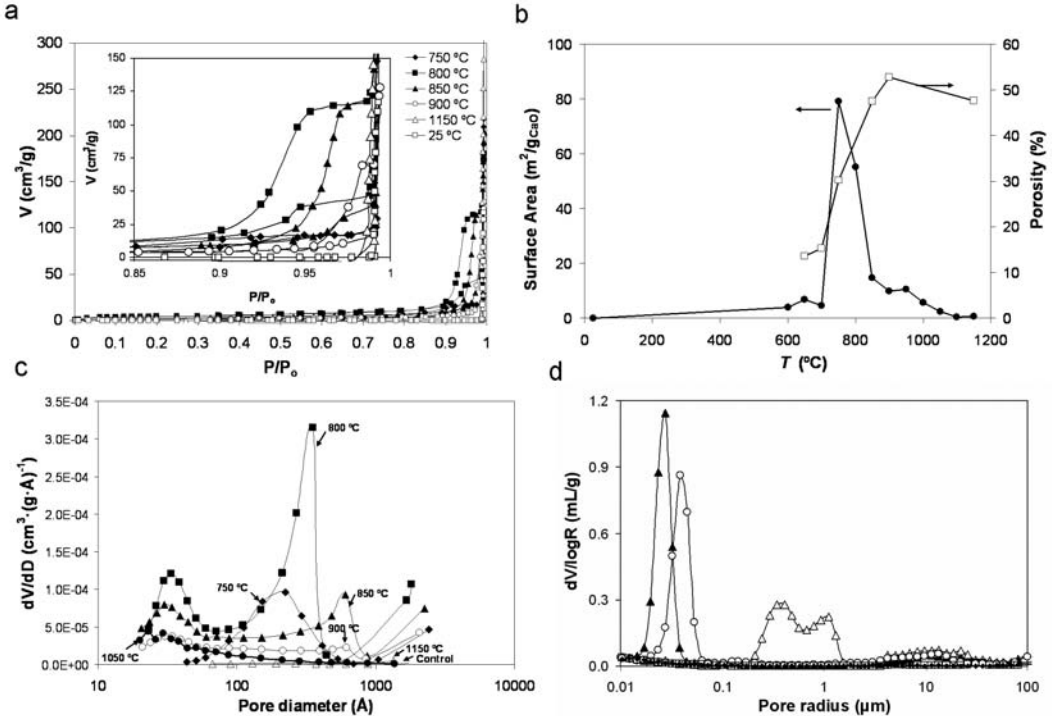

FIGURE 9. Surface area and porosity of calcite pseudomorphs: (**a**) N_2 adsorption isotherms of Iceland spar before and after calcinations at different temperatures. Inset shows details of hysteresis loops; (**b**) evolution of surface area (BET analysis of N_2 adsorption isotherms) and porosity (mercury intrusion porosimetry) of Iceland spar crystals calcined at different temperatures; (**c**) BJH plots and (**d**) mercury intrusion porosimetry curves showing pore-size distribution of Iceland spar crystals heated at different temperatures. Legend: uncalcined (open square) and calcite calcined at 750 °C (filled diamond), 800 °C (filled square), 850 °C (filled triangle), 900 °C (open circle), 1050 °C (filled circle), and 1150 °C (open triangle).

starting calcite crystals (Fig. 9b) and the absence of micro- and mesopores in the BJH pore-size distribution plots (Fig. 9c). After heating the crystals up to 750 °C, the isotherm changed to type-IV (i.e., with hysteresis loop), as reported elsewhere (Beruto et al. 1980). At this point ($\alpha = 0.11$), the maximum surface area (79.2 mg^2/g) was reached (Fig. 9b). This value is nearly double than those typically reported for calcite decomposition in air (e.g., 42 mg^2/g, Glasson 1958; 51 mg^2/g, Obst et al. 1978). The discrepancy may be associated with the fact that most previous studies do not normalize the surface area with respect to the fraction decomposed at a given *T*. Interestingly, the maximum surface area here reported approaches the typical values (89–104 mg^2/g) obtained following decomposition in vacuum (Ewing et al. 1979; Beruto et al. 1980; Borgwardt et al. 1986; Fuller and Yoos 1987). This also shows that P_{CO_2} does not influence the decomposition mechanism during the initial stage. The isotherms show a H_1 hysteresis loop (Sing et al. 1985) associated with capillary condensation in mesopores of cylindrical or tubular geometry. This is in good agreement with our FESEM and TEM observations showing a nearly parallel arrangement of needle- or rod-shaped submicrometer-sized CaO crystals separated by mesopores (initially with size ca. 5–10 nm). These results are very similar to those reported by Beruto et al. (1980, 1983, 1984, 2004), despite the fact that they studied the pore structure of $CaCO_3$ thermally decomposed in vacuum.

Samples with H_1 hysteresis loop often present a narrow distribution of pore sizes, as shown by the BJH plots (Fig. 9c). Three main classes of pores were detected: (1) pores (3 nm in size) that are close to the micropore size, and possibly correspond to pores between nascent CaO nanocrystals prior to coalescence (see TEM results); (2) mesopores (pores that are 30 nm in size) that are responsible for the hysteresis loop; they were identified by FESEM and TEM as pores between isolated CaO crystals with the same orientation in a domain and were produced after collapse of the CaO nanostructure following oriented aggregation; and (3) macropores (>50 nm in size) that could not be measured by N_2 adsorption but were detected by MIP (see below) and correspond to pores between iso-oriented domains that transform into individual larger crystals as sintering progresses with increasing *T*, as observed with FESEM and TEM. Pores of type 1 and 2 are responsible for the high surface area of $CaCO_3$ pseudomorphs. The closing of these mesopores with increasing *T* (from 750 to 850 °C) is responsible for both the significant reduction in surface area (Fig. 9b) and micropore volume, and the shift of the second relative maximum in BJH pore-size distribution toward higher values of pore size (Fig. 9c). Contrary to what was stated by Borgwardt et al. (1986) and Borgwardt (1989) such shift is not solely due to sintering, but rather to the combination of oriented aggregation (diffusionless) and sintering. While the former mechanism operates at $T < 850$ °C, the latter is more important at $T > 850$ °C.

Figure 9d shows MIP pore-size distribution (PSD) curves for calcite pseudomorphs calcined at different *T*. A clear PSD shift toward larger pore sizes with increasing calcination *T* was observed. The amount of nanopores (PSD maximum ca. 20 nm at 850 °C) was reduced and micrometer-sized pores opened up (ca. 0.3–2 μm in diameter at 1150 °C) as sintering progressed. A small volume of larger pores (ca. 10 μm in diameter) developed early during calcinations. This latter feature of PSD curves is interpreted as cracks developed upon calcite decrepitation (cracks observed with the FESEM). In parallel to the changes in PSD, a change in porosity was detected with the MIP. Calcite pseudomorphs calcined at 900 °C yielded a porosity of 53%, a value close to the theoretical maximum of 54.2% (Fig. 9b). Borgwardt (1989) has shown that the overall porosity of calcite pseudomorphs does not change significantly during the initial stages of decomposition when almost no shrinking is detected. However, a significant reduction in surface area occurred as observed here. The author proposes that a concentration of "grain clusters" limited by macropores should have developed following sintering. Our FESEM observation of calcite pseudomophs (Fig. 3) confirms that such a concentration of "grain clusters" takes place. However, this textural feature was explained by an oriented aggregation coarsening mechanism rather than the standard sintering proposed by Borgwardt (1989). Finally, at the maximum *T* reached (1150 °C) the porosity was reduced to 47%, which is a clear indication of the existence of sintering and associated shrinking (McClellan and Eades 1970).

Overall, N_2 sorption and MIP measurements, which enable the measurement of the smaller and larger pores, respectively, confirm microscopy observations of the textural evolution of CaO aggregates. However, with a few exceptions, MIP porosity values do not match those determined from DIA of FESEM and TEM images, although the trend in porosity variation (i.e., reduction with *T*) is similar. It appears that porosity data obtained from DIA of electron microscopy images (that typically correspond to very small surfaces) are not fully representative of the bulk solid. In the case of FESEM, the lower porosity values determined by means of DIA if compared with MIP, could also be associated with the fact that a significant amount of porosity must have been contributed by pores which were too small to quantify with this technique.

Kinetic analysis

Figure 10a shows α vs. T_α plots for Iceland spar decomposition obtained at heating rates of 2, 5, 10, and 15 K/min. Figure 10b shows the variation of apparent activation energy (E_α) vs. the extension of the reaction (α). This latter plot revealed a dependence of E_α on the transformation degree, which is an indication of the complex character of this process.

In a first step ($\alpha < 0.2$, 730 °C at 2 °C/min), the apparent activation energy increases with the decomposition degree, reaching a maximum value of 205 ± 10 kJ/mol ($\ln A = 20.6$ s^{-1}). For $\alpha > 0.2$, E_α slightly decreases with the extension of the reaction, reaching a value of 176 ± 9 kJ/mol ($\ln A = 17.2$ s^{-1}). Both the maximum and minimum E_α values here reported are in good agreement with those most commonly reported in the literature (Maciejewski and Reller 1987). They are however, much smaller than the 493 kJ/mol reported by L'vov et al. (2002). Note however, that the calculation method used by these authors assumes the formation of a gaseous product that condenses into the solid product. We have found no evidence for the existence of such a CaO gas under our experimental conditions. The change in E_α values that we have observed may be due to a change in the rate controlling mechanism as the reaction progresses toward the core. Three rate controlling processes are possible: heat transfer

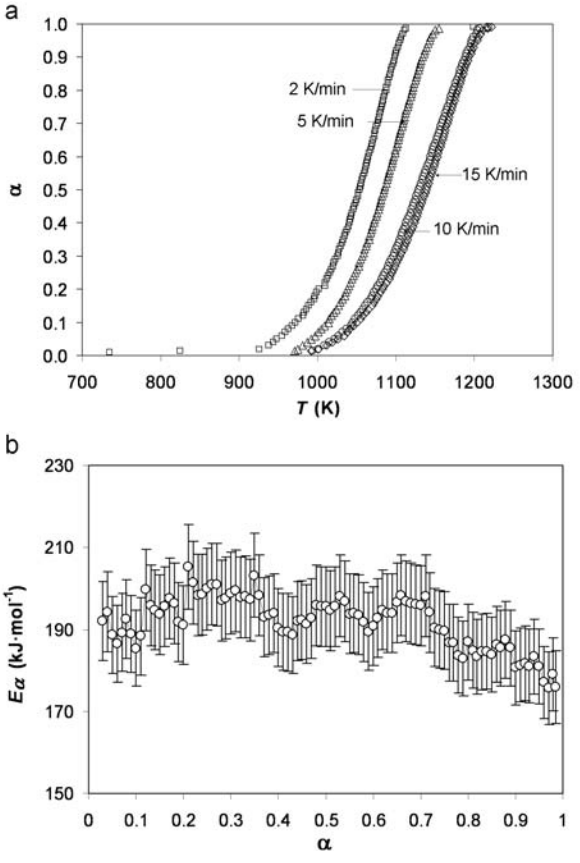

FIGURE 10. Kinetic results: (**a**) α vs. T_α plots for calcite decomposition obtained at heating rates of 2 K/min (open square), 5 K/min (triangle), 10 K/min (open circle), and 15 K/min (open diamond); (**b**) plot of E_α vs. α for calcite decomposition calculated by the FWO method.

to the reaction interface, chemical reaction, and CO_2 diffusion through the product layer (Satterfield and Feakes 1959). The relative importance of each process seems to depend on the experimental conditions. In our case, and according to the E_α vs. α curve, it seems plausible that in the initial steps of the process ($\alpha < 0.2$), diffusion controls the reaction; therefore, as the thickness of the product layer increases, the resistance against CO_2 diffusion increases and, as a consequence, the activation energy also increases. The development of a new phase with a lower molar volume in the early stages of the thermal decomposition leads to the formation of a mesoporous structure constituted by CaO crystals separated in domains with different orientations (see previous section) where CO_2 liberated from the reaction interface may be trapped (adsorbed), reducing the overall reaction rate and increasing the activation energy (Beruto et al. 2004). Adsorption of CO_2 in high-surface area (nanoporous) CaO has been reported (Beruto et al. 2004). Searcy and Beruto (1978) have suggested that shear-induced transitions during $CaCO_3$ thermal decomposition occur very rapidly following depletion of CO_2 at the reaction front. Thus, the authors conclude that the rate limiting process should be condensed phase diffusion of CO_2, at least at the very beginning of the decomposition process. At $\alpha > 0.20$, oriented aggregation of CaO crystals plus limited

TABLE 2. Results of the model-fitting method for the lower heating rate (2 K/min)

	E_1	A_2	A_3	A_4	B_1	R_2	R_3
E (kJ/mol)	–84.02	84.57	52.79	36.90	36.19	119.80	139.84
ln (A)	–13.04	6.03	2.05	–0.03	1.84	9.33	11.40
r^2	0.9254	0.5856	0.3855	0.2457	0.1325	0.8905	0.8873
	D_1	D_2	D_3	D_4	F_1	F_2	F_3
E (kJ/mol)	203.42	250.38	252.34	–271.98	179.90	300.10	420.30
ln (A)	18.20	24.04	28.28	25.21	17.46	32.34	47.91
r^2	0.8991	0.9358	0.8873	0.9385	0.8083	0.7162	0.6744

sintering (taking place simultaneously to further decomposition) led to the partial closure of the smaller pores between CaO crystals and to shrinkage of the different domains formed, which resulted in the formation of macropores. These are paths through which CO_2 can easily escape. The minimum value of apparent activation energy reached at this stage (176 ± 9 kJ/mol) is close to that reported for the reaction enthalpy: ΔH = 177.8 kJ/mol (Fuller and Yoos 1987). Thus, it seems that during most of the $CaCO_3$-CaO transformation, there is no significant resistance against CO_2 diffusion and, therefore, chemical reaction controls the kinetics of the process.

The application of the model-fitting method to raw TGA data further confirmed the idea that not a single mechanism is ruling the process. In fact, none of the different equations proposed for $f(\alpha)$ (Table 1) yielded a good fitting of TGA data over the whole range of conversions (Table 2). It is important to note that, although the value of the correlation coefficient was below 0.9, D_1 and F_1 mechanisms yield apparent E_α values (203 and 180 kJ/mol, respectively) and ln$A$ (18.2 and 17.5 s^{-1}, respectively) very similar to the maximum and the minimum values of activation energy and corresponding pre-exponential factors calculated using the FWO method, especially at the lowest heating rate (2 K/min). Therefore, it seems that during the thermal decomposition both D_1-diffusion (from the reaction interface toward the surface of calcite pseudomorph), and chemical reaction, F_1 (first order), are controlling the process. Initially, the first mechanism is predominant, while later on when the reaction is established, the chemical reaction is the rate limiting process. Maitra et al. (2007) have recently reported that two-dimensional diffusion (D_2) is the overall controlling mechanism. The authors calculated an effective activation energy E_α of 224.46 kJ/mol, which is slightly higher than that obtained here when the process is diffusion-controlled (i.e., for $\alpha < 0.20$). The authors used a TGA under N_2 static conditions, which reportedly overemphasize diffusion as the rate-limiting step (Wang and Thomson 1995). Note that in our case, the high flow-rate of the purging gas used in the TGA analysis could significantly reduce the effect mentioned above; however, it is not known if it was fully eliminated. Thus, it could be argued that the initial ($\alpha < 0.2$) diffusion-controlled stage could be an experimental artifact. However, there is strong evidence suggesting that except for the very first atomic layer of a solid, degassing is delayed until the domain boundaries undergo some form of coalescence resulting in an interconnected network which opens fast diffusion pathways for the gas molecules to migrate to the outer surface (Chaix-Pluchery et al. 1983). On the other hand, it has been reported that chemical reaction should be the rate-limiting step in calcite thermal decomposition when heat/mass transfer and diffusion effects are minimized (reducing

sample size and performing decomposition in vacuum) (Beruto and Searcy 1974; Criado and Ortega 1992; Wang and Thomson 1995). In such a case, a first-order reaction (F_1) is the controlling mechanism, as observed here for $\alpha > 0.20$. The good kinetic fit with the first order equation for most of the transformation process is consistent with a homogeneous mechanism (Galwey and Laverty 1993), i.e., the overall decomposition mechanism must be of the shear-type or topotactic (Kim et al. 1987; Beruto et al. 2004).

Mechanisms of thermal decomposition of calcite

Both the kinetic analysis and the analytical results presented and discussed above point to a topotactic (i.e., structurally controlled) mechanism as the responsible for the thermal transformation of calcite into CaO. In contrast to earlier kinetic studies pointing to nucleation and growth as the dominant mechanism in solid-state endothermic decomposition reactions of the type $A_{solid} = B_{solid} + C_{gas}$ (Niepce and Watelle-Marion 1973), there is growing evidence suggesting that in most cases such reactions are topotactic (shear-transformations) (Figlarz et al. 1990). This is, for instance, the case of the decomposition of many hydroxides and oxy-hydroxides (e.g., Dasgupta 1961; Chaix-Pluchery et al. 1983; Kim et al. 1987; Figlarz et al. 1990). Both dolomite- and calcite-type carbonates also show topotactic decomposition relationships. Such is the case of dolomite $MgCa(CO_3)_2$ (Carter and Busek 1985), ankerite $MgFe(CO_3)_2$ (Dasgupta and Phil 1965), siderite $FeCO_3$ (Dasgupta 1961), magnesite $MgCO_3$ (Dasgupta 1964; Singh Dev 1972; Kim et al. 1987), and otavite $CdCO_3$ (Floquet and Niepce 1978). In the case of calcite-type carbonates, many possible topotactic orientation relationships have been proposed since the 1960s. In his pioneering study on the thermal decomposition of magnesite, Dasgupta (1964) reported that there was a strong structural similarity between the alternate metal/carbonate layer along the threefold axis of the carbonate and the metal/oxygen layers along the threefold axes in the face-centered cubic structure of product oxide. Such a simple structural similitude led to the assumption that the most plausible orientation relationship between carbonate and oxide was $[001]_{carbonate}//[111]_{oxide}$ (e.g., Kim et al. 1987). However, a close examination of the structures of calcite and CaO (Figs. 11a and 11b) along those directions shows that significant ion displacement will be required to fulfill such a topotactic relationship. The very complete XRD study by Floquet and Niepce (1978) on the orientation relationships between $CdCO_3$ (another calcite-type carbonate) and the product CdO shows that the simplifying assumption made by Dasgupta (1964), as well as by McTigue and Wenk (1985) and Kim et al. (1987) later on, might not be correct. Floquet and Niepce (1978) found that the (0001) plane of $CdCO_3$ did not yield the (111) plane of CdO; instead, the [001] axis of the carbonate became the $[\bar{1}40]$ axis of three disjoined sets of oxide crystallites oriented at 120°. Although we have observed none of these topotactic relationships, our results show that the thermal decomposition of calcite leads to several (up to four) disjoined sets of oriented oxide crystallites on each $\{10\bar{1}4\}$ face in agreement with the Floquet and Niepce (1978) conclusion about the variety of orientation relationships resulting from these topotactic reactions. Below, a model explaining how these four sets of CaO crystals form on each calcite cleavage plane is presented and discussed.

Figure 11c shows the structure of calcite $(10\bar{1}4)$ plane. The $[\bar{4}41]$ and symmetrically equivalent $[48\bar{1}]$ directions that are parallel to the edges of the $\{10\bar{1}4\}$ rhombohedron are characterized by chains of alternating Ca^{2+} and CO_3^{2-} ions forming one set of important calcite periodic bond chains or PBCs (Paquette and Reeder 1995). The other two sets of PBCs run along <010> and $<2\bar{2}1>$. Our SAED results show that the [841] direction, or any equivalent $<\bar{4}41>$ direction, corresponds to the $[1\bar{1}0]$ (or equivalent <110>) direction of CaO crystals in calcite pseudomorphs. In contrast, $<110>_{CaO}$ directions are characterized by chains of Ca ions parallel to oxygen chains. Thus, there is not a straightforward structural similitude between reactant and product in such directions. However, if the conversion of calcite into CaO with an orientation equivalent to that of set 2 in Figure 7d occurs by lost of CO_2 accompanied by limited atom displacement and shrinking parallel to $[\bar{4}41]_{calcite}$, the parent $(10\bar{1}4)$ plane readily yields the product $(1\bar{1}0)$ plane as depicted in the sequence shown in Figures $11d_1$–$11d_3$. Such shrinkage is necessary because the Ca-$CO_3^=$ bond length along $[\bar{4}41]_{calcite}$ is 3.212 Å, while the Ca-O distance along $<001>_{CaO}$ is 2.405 Å (i.e., a reduction of 25.1%). Strain effects may limit such a length reduction to a few unit cells of the product without loss in continuity. This explains why the thickness of nascent CaO crystals is ca. 5 nm, i.e., about 10 unit cells. As shown by our TEM-SAED analysis, CaO crystals are elongated along $[110]_{CaO}$. This is because, as depicted in Figure 11c, no significant change in bond length is required along $[48\bar{1}]_{calcite}$ upon conversion into $[110]_{CaO}$. Each Ca-$CO_3^=$ bond along $[48\bar{1}]_{calcite}$, which upon CO_2 loss turns into a Ca-Ca bond by displacement and shrinking nearly parallel to $[\bar{4}41]_{calcite}$, has a length of 3.212 Å, while the Ca-Ca bond length along $[110]_{CaO}$ is 3.401 Å, i.e., a 5.9% increase in length. The above described transformation also involves a 15° rotation of the product $(1\bar{1}0)$ plane with respect to the parent $(10\bar{1}4)$ plane to fulfill the observed orientation relationship $[1\bar{1}0]_{CaO}//[841]_{calcite}$. Regarding the third dimension of these CaO crystals, one has to consider that by similar atom displacement in the $(10\bar{1}4)$ layer below the surface as that depicted in Figure 11d, plus 2.93 Å displacement of the product plane along $[112]_{CaO}$, the parent $(10\bar{1}4)_{calcite}$ plane will transform into $(2\bar{2}0)_{CaO}$. This transformation will be followed by a 43.9% shrinking from 3.03 Å (i.e., the calcite d_{104} spacing) to 1.70 Å (i.e., d_{220} spacing of CaO). Thus, the product crystals can grow toward the core of the calcite crystal with $(0\bar{1}14)_{calcite}\perp(110)_{CaO}$ and $[1\bar{1}0]_{CaO}//[841]_{calcite}$. The shrinkage along $[\bar{4}41]_{calcite}$ and $[841]_{calcite}$ is responsible for the nanoporosity developed between lime nanocrystals. The slight length increase along $[110]_{CaO}$ will be fully compensated by the different orientation among contiguous sets of iso-oriented lime crystal bundles (shown in Fig. 3c). Overall, the calculated shrinkage in 3D is 55.5%, in good agreement with the theoretical porosity associated to this transformation (i.e., 54.2%). The above described transformation can take place either along $[\bar{4}41]_{calcite}$ or along its equivalent $[48\bar{1}]_{calcite}$ direction on the same rhombohedral $(10\bar{1}4)$ face. This will lead to the two sets of CaO crystals denoted as 2 and 4 (Fig. 7d), which are elongated along [110] and oriented at ~75° on each $\{10\bar{1}4\}_{calcite}$ face as determined by means of FESEM, TEM-SAED, and 2D-XRD analyses. In the case of crystals showing the other two orientation relationships,

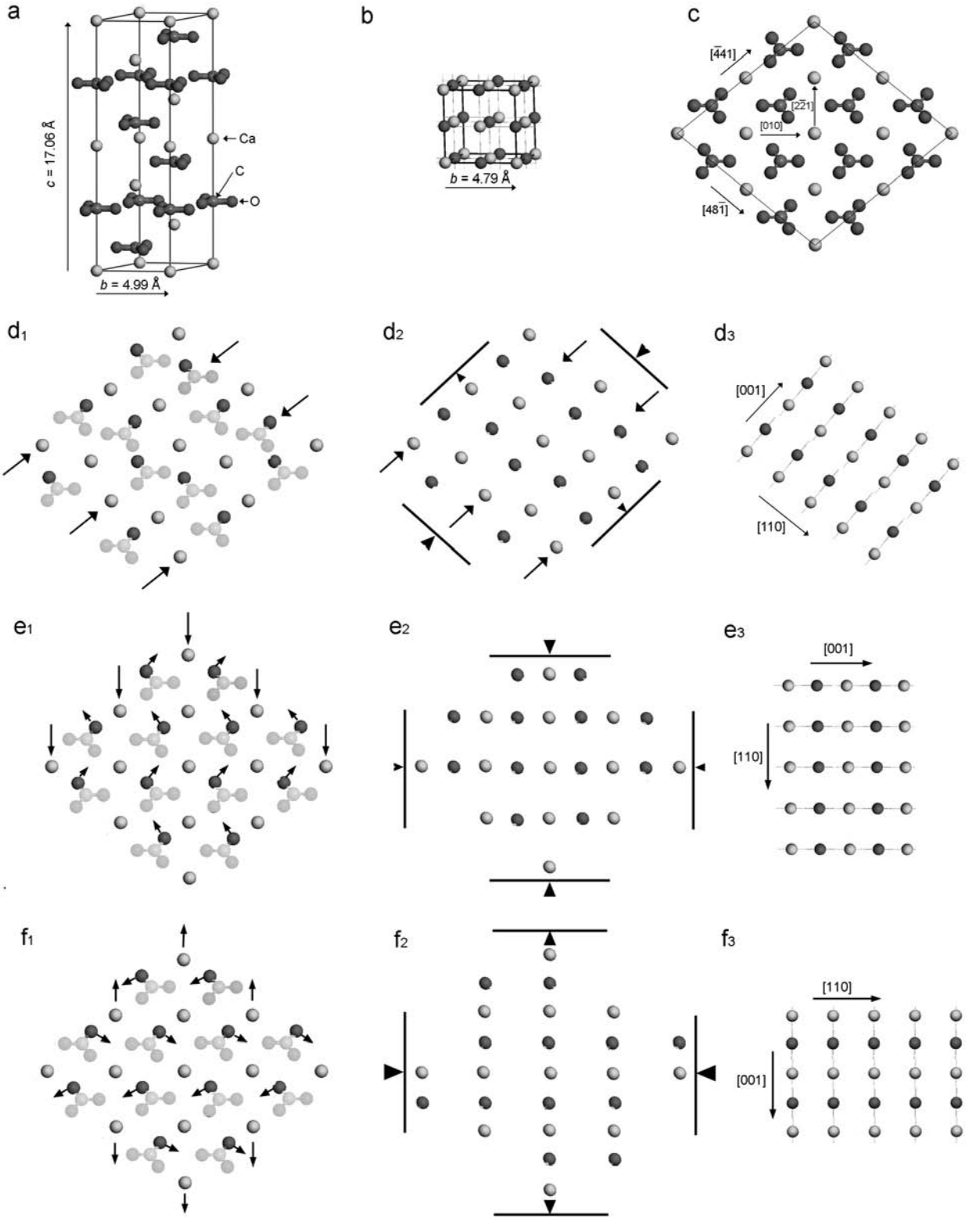

FIGURE 11. Scheme representing the structure of calcite (**a**) hexagonal cell and CaO (**b**), as well as the structural evolution of the $(10\bar{1}4)$ plane of calcite (**c**), upon loss of CO_2 leading to CaO crystals with: (**d**) orientation (2); (**e**) orientation (3) and (**f**) orientation (1). In all three cases the sequence (from left to right) shows atom movement (arrows) and cell contraction (or expansion) (arrowheads + bar) resulting in the structure of the $(1\bar{1}0)$ plane of CaO. Faded parts of CO_3^{2-} groups represent those atoms that are lost as CO_2 upon calcite thermal decomposition.

namely sets 1 and 3 in Figure 7d, CO_2 loss and associated atom displacement will take place according to the sequences shown in Figure 11e_1–11e_3 (for set 3) and Figure 11f_1–11f_3 (for set 1). In the case of set 3, the transformation involves a shrinkage of 16% along $[2\bar{2}1]_{calcite}$ and 4% along $[010]_{calcite}$. In the third direction, i.e., along $[841]_{calcite}$, the shrinkage is similar to that calculated for set 2 (as well as 4): i.e., a 43.9%. In the case of set 3, atom displacement within the $(10\bar{1}4)$ plane located just underneath the surface is similar to that depicted in Figure 11e, plus a displacement of the whole product plane similar to that described for set 2.

Overall, the 3D shrinkage leads to a porosity of 54.9%, i.e., nearly the theoretical one. In the case of set 1, there is a 31.8% shrinkage along $[010]_{calcite}$, and a 43.9% shrinkage along $[841]_{calcite}$. However, there is an expansion of 18% along $[2\bar{2}1]_{calcite}$. Although such a relatively high degree of expansion does not prevent the formation of set 1, it does not favor it either. This explains why such a set is the less abundant in Figure 7d. Regarding CaO growth along $[841]_{calcite}$, shrinkage for set 1 will be similar to that calculated for the other sets: i.e., a 43.9%. Atom displacement within the $(10\bar{1}4)$ plane underneath the surface will also follow the same sequence of the other sets. All in all, the total volume reduction is 54.9%, as in the case of set 3. The four sets of transformations described above would take place along equivalent directions on each of the six $\{10\bar{1}4\}$ rhombohedral faces of calcite while the reaction front advances from the surface to the core of the calcite rhombohedron.

This topotactic transformation is triggered by the loss of CO_2 molecules formed at the surface of $\{10\bar{1}4\}_{calcite}$ faces. Shannon (1964) states that rotational energy is involved in the $CO_3^=$ loss of CO_2 via the formation of an activated complex of the type $O^= \cdots CO_2$, which is consistent with observations of $CO_3^=$ ions replacement by $O^=$ ions on a calcite surface monolayer (Beruto et al. 2004). Rotational activity followed by degassing of CO_2 is facilitated when carbonate groups are nearly normal to the calcite surface (Fox and Soria-Ruiz 1970), as it is the case for the calcite cleavage plane (Fig. 11c). The two outermost O atoms in the carbonate groups sticking out of the cleavage plane would be the ones most easily lost (Figs. 11d_1–11f_1). Once CO_2 is lost, the surface layer will undergo a steady-state, diffusionless retreat by collapsing, due to strain accumulation, into the oriented array of CaO nanorods and pores here observed with the FESEM and TEM. Stress release will result in the ejection of the remaining CO_2 that will diffuse outward leaving a lacunar structure behind, which is reorganized by cooperative, limited movements of the atoms in the product phase (at the unit-cell scale) as explained above and depicted in Figures 11d–11f. Such a limited atom displacement cannot be mistaken for a diffusion process (random walk) (Bertrand 1978). The absence of diffusion is consistent with the observed in situ transformation of calcite into four oriented arrays of CaO nanocrystals following electron irradiation in the TEM. Mechanical stress accumulated among crystals due to the molar volume differences between reactant and product results in the splitting of the product crystals, leaving the observed mesoporous structure. Afterward, oriented aggregation of nascent CaO nanocrystals with nearly equal orientation, results in the closing of mesopores. Overall, the reaction progresses via the existence of an (energetically and mechanically) unstable nanostructured intermediate product. Finally, sintering leads to the development of micrometer-sized pores. During all this structural evolution, the initial orientation of the nascent CaO crystals is preserved, up to the stage of advanced sintering observed at 1150 °C. Sintering will take place at a faster rate in the presence of CO_2 due to its catalytic role (Beruto et al. 2004). P_{CO_2} will also have an important effect on the calcite decomposition T and its decomposition rates (Zhong and Bjerle 1993). However, our in-situ and ex-situ TEM observations show that P_{CO_2} does not affect the topotactic decomposition mechanism.

In summary, both the textural and kinetic results presented and discussed show that the thermal decomposition of calcite is homogeneous and topotactic in nature, and do not depend on the experimental conditions (e.g., P_{CO_2}, crystal size, or type of energy used for the activation of the reaction). These results shed light into the mechanisms of calcite calcination and help understand the textural evolution of the product CaO. Such knowledge has allowed us to propose a novel topotactic mechanism for the calcite/CaO transformation, and may help constrain calcination conditions to achieve the best properties (in terms of crystal size, surface area, porosity, and reactivity) for industrial applications. Our model for the thermal decomposition of calcite may also help establish crystallographic constraints for possible relationships between reactant and product, in order to interpret textural relationships found in natural samples (e.g., Martian meteorites).

Acknowledgments

This work has been financially supported by the Ministerio de Educación y Ciencia, Spain, under Contract MAT2006-00578. Financial support has also been provided by the research group RNM-179 (Junta de Andalucía, Spain). We thank the personnel of the Centro de Instrumentación Científica of the Universidad de Granada for assistance during TGA, TEM, and FESEM analyses.

References cited

Barber, D.J. and Scott, E.R.D. (2003) Transmission electron microscopy of minerals in the martian meteorite Allan Hills 84001. Meteoritics and Planetary Science, 38, 831–848.

Barrett, E.P., Joyner, L.S., and Halenda, P.P. (1951) The determination of pore volume and area distributions in porous substances: I. Computations with nitrogen isotherms. Journal of the American Chemical Society, 73, 373–380.

Bertrand, G. (1978) Comments on "Kinetics of endothermic decomposition reactions. 2. Effect of the solid and gaseous product." Journal of Physical Chemistry 82, 2536–2537.

Beruto, D. and Searcy, A.W. (1974) Use of Langmuir method for kinetic studies of decomposition reactions: calcite ($CaCO_3$). Journal of the Chemical Society, Faraday Transactions I, 70, 2145–2153.

——— (1976) Calcium oxides of high reactivity. Nature, 263, 221–222.

Beruto, D., Barco, L., Searcy, A.W., and Spinolo, G. (1980) Characterization of the porous CaO particles formed by decomposition of $CaCO_3$ and $Ca(OH)_2$ in vacuum. Journal of the American Ceramic Society, 63, 439–443.

Beruto, D., Barco, L., and Searcy, A.W. (1983) Rearrangement of porous CaO aggregates during calcite decomposition in vacuum. Journal of the American Ceramic Society, 66, 893–896.

——— (1984) CO_2-catalyzed surface-area and porosity changes in high-surface-area CaO aggregates. Journal of the American Ceramic Society, 67, 512–515.

Beruto, D., Searcy, A.W., and Kim, M.G. (2004) Microstructure, kinetic, structure, thermodynamic analysis for calcite decomposition: Free-surface and powder bed experiments. Thermochimica Acta, 424, 99–109.

Best, M.G. (1982) Igneous and Metamorphic Petrology. Freeman, New York.

Borgwardt, R.H. (1985) Calcination kinetics and surface area of dispersed limestone particles. AIChE Journal, 31, 103–110.

——— (1989) Calcium oxide sintering in atmospheres containing water and carbon dioxide. Industrial Engineering Chemistry Research, 28, 493–500.

Borgwardt, R.H., Roache, N.F., and Bruce, K.R. (1986) Method for variation of grain size in studies of gas-solid reactions involving CaO. Industrial Engineering Chemistry Fundamentals, 25, 165–169.

Boynton, R.S. (1980) Chemistry and Technology of Lime and Limestone, 2nd edition. Wiley-Interscience, New York.

Brunauer, S., Emmett, P.H., and Teller, E. (1938) Adsorption of gases in multimolecular layers. Journal of the American Chemical Society, 60, 309–319.
Burrage, B.J. and Pitkethly, D.R. (1969) Aragonite transformations observed in the electron microscope. Phisica Status Solidi, 32, 399–405.
Carter, E.D. and Buseck, P.E. (1985) Mechanism of decomposition of dolomite, $Ca_{0.5}Mg_{0.5}CO_3$, in the electron microscope. Ultramicroscopy 18, 241–252.
Chaix-Pluchery, O., Bouillot, J., Ciosmak, D., Niepce, J.C., and Freund, F. (1983) Calcium-hydroxide dehydration early precursor states. Journal of Solid State Chemistry, 50, 247–255.
Criado, J.M. and Ortega, A. (1992) A study of the influence of particle size on the thermal decomposition of $CaCO_3$ by means of constant rate thermal analysis. Thermochimica Acta, 195, 163–167.
Dasgupta, D.R. (1961) Topotactic transformations in iron oxides and oxyhydroxides. Indian Journal of Physics, 35, 401–419.
——— (1964) Oriented transformation of magnesite. Indian Journal of Physics, 38, 623–626.
Dasgupta, D.R. and Phil, D. (1965) The transformation of ankerite during thermal treatment. Mineralogical Magazine, 35, 634–639.
Dash, S., Kamruddin, M., Ajikumar, P.K., Tyagi, A.K., and Raj, B. (2000) Nanocrystalline and metastable phase formation in vacuum thermal decomposition of calcium carbonate. Thermochimica Acta, 363, 129–135.
Elert, K., Rodriguez-Navarro, C., Sebastian Pardo, E., Hansen, E., and Cazalla, O. (2002) Lime mortars for the conservation of historic buildings. Studies in Conservation, 47, 62–75.
Ewing, J., Beruto, D., and Searcy, A.W. (1979) The nature of CaO produced by calcite powder decomposition in vacuum and in CO_2. Journal of the American Ceramic Society, 62, 580–584.
Figlarz, M., Gérand, B., Delahaye-Vidal, A., Dumont, B., Harb, F., Coucou, A., and Fievet, F. (1990) Topotaxy, nucleation and growth. Solid State Ionics, 43, 143–170.
Fischer, H.C. (1955) Calcination of calcite: II, Size and growth rate of calcium oxide crystallites. Journal of the American Ceramic Society, 38, 284–288.
Floquet, N. and Niepce, J.C. (1978) Threefold transformation twin in the topotactic decomposition of cadmium carbonate crystals. Journal of Materials Science, 13, 766–776.
Fox, P.G. and Soria-Ruiz, J. (1970) Dislocations and the thermal reactivity of calcite. Proceedings of the Royal Society London A, 314, 429–441.
Fuller, E.L. and Yoos, T.R. (1987) Surface properties of limestones and their calcination products. Langmuir, 3, 753–760.
Galwey, A.K. and Brown, M.E. (1998) Kinetic background to thermal analysis. In M.E. Brown, Ed., Handbook of Thermal Analysis and Calorimetry, Volume 1, Principles and Practice, Chapter 3, p. 147–224. Elsevier Scientific, Amsterdam.
Galwey, A.K. and Laverty, G. (1993) A kinetic and mechanistic study of the dehydroxylation of calcium hydroxide. Thermochimica Acta, 228, 359–378.
Glasson, D.R. (1958) Reactivity of lime and related oxides: I. Production of calcium oxide. Journal of Applied Chemistry, 8, 793–797.
——— (1961) Reactivity of lime and related oxides. VII Crystal size variations in calcium oxide produced form limestone. Journal of Applied Chemistry, 11, 201–206.
Grapes, R. (2006) Pyrometamorphism. Springer, Berlin.
Han, R., Shimamoto, T., Hirose, T., Ree, J.-H., and Ando, J. (2007) Ultralow friction of carbonate faults caused by thermal decomposition. Science, 316, 878–881.
Harker, R.I. and Tuttle, O.F. (1955) Studies in the system CaO-MgO-CO_2. Part 1: The thermal dissociation of calcite, dolomite and magnesite. American Journal of Science, 253, 209–224.
Howard, S.A. and Preston, K.D. (1989) Profile fitting of powder diffraction patterns. In D.L. Bish and J.E. Post, Eds., Modern Powder Diffraction, 20, p. 217–276. Reviews in Mineralogy, Mineralogical Society of America, Chantilly, Virginia.
Kim, M.G., Dahmen, U., and Searcy, A.W. (1987) Structural transformations in the decomposition of $Mg(OH)_2$ and $MgCO_3$. Journal of the American Ceramic Society, 70, 146–154.
Kingery, W.D. (1960) Introduction to Ceramics. Wiley, New York.
Klimenkov, M., Matz, W., Nepjiko, S.A., and Lehmann, M. (2001) Crystallisation of Ge nanoclusters in SiO_2 caused by electron irradiation in TEM. Nuclear Instruments and Methods in Physics Research B, 179, 209–214.
Maciejewski, M. and Ostwald, H.R. (1985) Morphological observations on the thermal decomposition of calcium carbonate. Thermochimica Acta, 85, 39–42.
Maciejewski, M. and Reller, A. (1987) How (un)reliable are kinetic data of reversible solid-state decomposition processes? Thermochimica Acta, 110, 145–152.
Maitra, S., Bandyopadhyay, N., Das, S., Pal, A.J., and Pramanik, J. (2007) Non-isothermal decomposition kinetics of alkaline earth metal carbonates. Journal of the American Ceramic Society, 90, 1299–1303.
Martín-Ramos, J.D. (2004) XPowder: A software package for powder X-Ray diffraction analysis, Version 2004.03, http://www.xpowder.com.
McClellan, G.H. and Eades, J.L. (1970) The textural evolution of limestone calcines. In The Reaction Parameters of Lime, p. 209–227. ASTM Special Publication 472, American Society for Testing and Materials, Philadelphia.
McTigue, J.W. and Wenk, H.R. (1985) Microstructures and orientation relationships in the dry-state aragonite-calcite and calcite/lime phase transformations. American Mineralogist, 70, 1253–1261.
Mikhail, R.S., Hanafi, S., Abo-el-Enein, S.A., Good, R.J., and Irani, J. (1980) Morphology and surface area changes in the thermal dissociation of Iceland spar. Journal of Colloid and Interface Science, 75, 74–84.
Niepce, J.C. and Watelle-Marion, G. (1973) A propos du concept de germination et croissance des germes dans le cas de reactions de déscomposition endothermiques du type solide 1 → solide 2 + gaz. Comptes Rendus de la Academie des Sciences Paris C, 276, 627–630.
Obst, K.H., Münchberg, W., and Rähder, M. (1978) Zur Erzeugung von aktivem Branntkalk. Zement-Kalk-Gips, 31, 373–385.
O'Keefe, J.D. and Ahrens, T.J. (1989) Impact production of CO_2 by the Cretaceous/Tertiary extinction bolide and the resultant heating of the Earth. Nature, 338, 247–249.
Paquette, J. and Reeder, R.J. (1995) Relationship between surface structure, growth mechanism, and trace element incorporation in calcite. Geochimica et Cosmochimica Acta, 59, 735–749.
Penn, R.L. and Banfield, J.F. (1998) Imperfect oriented attachment: Dislocation generation in defect-free nanocrystals. Science, 281, 969–971.
Powell, E.K. and Searcy, A.W. (1982) Surface-areas and morphologies of CaO produced by decomposition of large $CaCO_3$ crystals in vacuum. Journal of the American Ceramic Society, 65, C42–C44.
Rodriguez-Navarro, A.B. (2007) Registering pole figures using an X-ray single-crystal diffractometer equipped with an area detector. Journal of Applied Crystallography, 40, 631–634.
Rodriguez-Navarro, C., Ruiz-Agudo, E., Ortega-Huertas, M., and Hansen, E. (2005) Nanoestructure and irreversible colloidal behavior of $Ca(OH)_2$: Implications in cultural heritage conservation. Langmuir, 21, 10948–10957.
Ruiz-Agudo, E., Martin-Ramos, D., and Rodriguez-Navarro, C. (2007) Mechanism and kinetics of dehydration of epsomite crystals formed in the presence of organic additives. Journal of Physical Chemistry B, 111, 41–52.
Satterfield, C.N. and Feakes, F. (1959) Kinetics of the thermal decomposition of calcium carbonate. AIChE Journal 5, 115–122.
Searcy A.W. and Beruto, D. (1978) Response to comments on "Kinetics of endothermic docomposition reactions." 2. Effects of solid and gaseous products. Journal of Physical Chemistry, 82, 2537–2538.
Shannon, R.D. (1964) Activated complex theory applied to the thermal decomposition of solids. Transactions of the Faraday Society, 60, 1902–1913.
Sing, K.S.W., Everett, D.H., Haul, R.A.W., Moscou, L., Pierotti, R.A., Rouquérol, J., and Siemieniewska, T. (1985) Reporting physisorption data for gas/solid systems with special reference to the determination of surface area and porosity. Pure and Applied Chemistry 57, 603–619.
Singh, A., Dash, S., Kamruddin, M., Ajikumar, P.K., Tyagi, A.K., Raghunathan, V.S., and Raj, B. (2002) Formation of nanocrystalline calcia by the decomposition of calcite. Journal of the America Ceramic Society, 85, 927–932.
Singh Dev, R. (1972) Topotaktische Phänomene bei der Calcinierung, Sulfatisierung und Chloridisierung einiger Karbonat-Einkristalle. Neues Jahrbuch für Mineralogie Monatshefte, 1, 12–22.
Spinolo, G. and Anselmi-Tamburini, U. (1989) Mechanism of low temperature calcite decomposition. Solid State Ionics, 32/33, 413–419.
Stanmore, B.R. and Gilot, P. (2005) Review: Calcination and carbonation of limestone during thermal cycling for CO_2 sequestration. Fuel Processing Technology, 86, 1707–1743.
Towe, K.M. (1978) Ultraestructure of calcite decomposition in vacuo. Nature, 274, 239–240.
Vyazovkin, S.V. and Dollimore, D.J. (1996) Linear and nonlinear procedures in isoconversional computations of the activation energy of nonisothermal reactions in solids. Journal of Chemical Information and Computer Sciences, 36, 42–45.
Vyazovkin, S.V. and Wight, C.A. (1997) Isothermal and nonisothermal reaction kinetics in solids: In search of ways toward consensus. Journal of Physical Chemistry A, 101, 8279–8284.
Wang, Y. and Thomson, W.J. (1995) The effects of steam and carbon dioxide on calcite decomposition using dynamic X-ray diffraction. Chemical Engineering Science, 50, 1373–1382.
Wenk, H.R., Barber, D.J., and Reeder, R.J. (1983) Microstructures in carbonates. In R.J. Reeder, Ed., Carbonates: Mineralogy and Chemistry, 11, p. 301–307. Reviews in Mineralogy, Mineralogical Society of America, Chantilly, Virginia.
Wilburn, F.W. and Sharp, J.H. (1993) The bed-depth effect in the thermal decomposition of carbonates. Journal of Thermal Analysis, 40, 133–140.
Zhong, Q. and Bjerle, I. (1993) Calcination kinetics of limestone and the microstructure of nascent CaO. Thermochimica Acta, 223, 109–120.

Manuscript received May 16, 2008
Manuscript accepted November 20, 2008
Manuscript handled by Hongwu Xu